Spin-orbit coupling in wurtzite heterostructures

Jiyong Fu [1,2] Poliana H. Penteado [2] Denis R. Candido [2,3,4] G. J. Ferreira [5] D. P. Pires,[2,6]
E. Bernardes [2] and J. C. Egues [2]

[1]*Department of Physics, Qufu Normal University, Qufu, Shandong 273165, China*
[2]*Instituto de Física de São Carlos, Universidade de São Paulo, 13560-970 São Carlos, São Paulo, Brazil*
[3]*Department of Physics and Astronomy, University of Iowa, Iowa City, Iowa 52242, USA*
[4]*Pritzker School of Molecular Engineering, University of Chicago, Chicago, Illinois 60637, USA*
[5]*Instituto de Física, Universidade Federal de Uberlândia, Uberlândia, Minas Gerais 38400-902, Brazil*
[6]*Departamento de Física Teórica e Experimental, Universidade Federal do Rio Grande do Norte,
59072-970 Natal, Rio Grande do Norte, Brazil*

A detailed derivation of the Rashba spin-orbit (SO) Hamiltonian for conduction electrons in wurtzite
heterostructures is lacking in the literature. Here we derive in a consistent and systematic way such an effective
Hamiltonian, valid for quantum wells, wires, and dots with arbitrary confining potentials and external magnetic
fields. We start from an 8×8 Kane model accounting for the s-p_z orbital mixing important to wurtzite structures,
but absent in zincblende, and apply both quasidegenerate perturbation theory (Löwdin partitioning) and the
folding down approach to derive an effective 2×2 Hamiltonian for conduction electrons. For bulk systems, our
derivation consistently yields the well-known linear-in-momentum bulk inversion asymmetry (BIA) Rashba-like
term, with SO coupling $\alpha_{\text{bulk}}^{\text{BIA}}$, entirely following from the s-p_z orbital mixing and in agreement with experiments.
We also obtain the correct *form* of the bulk Dresselhaus term, which is the same as that of the Rashba. However,
our calculated bulk Dresselhaus SO parameters γ and b are too small. Focusing on wurtzite quantum wells,
we perform a self-consistent Poisson-Schrödinger calculation in the Hartree approximation to determine all
the relevant SO couplings of the confined effective 2×2 electron Hamiltonian. Our total linear Rashba-type
SO Hamiltonian contains a structural inversion asymmetry (SIA) part, modulated by the Hartree, doping, and
external gate potentials of the wells, and, in contrast to zincblende structures, a confined Rashba-type contribution
induced by the BIA of the underlying wurtzite lattice. Our calculation shows this latter BIA term to be the
main contribution to the confined Rashba coupling in wurtzite wells. As a concrete example, we determine the
intrasubband (intersubband) Rashba α_ν (η) and linear Dresselhaus β_ν (Γ) SO coupling strengths for GaN/AlGaN
single and double wells with one and two occupied subbands ($\nu = 1, 2$). Since the linear Rashba and the
Dresselhaus terms have the same functional form, we can define a total effective SO coupling $\alpha_\nu^{\text{eff}} = \alpha_\nu + \beta_\nu$.
For the GaN/Al$_{0.3}$Ga$_{0.7}$N single well with one occupied subband we find $\alpha_1^{\text{eff}} = 7.16$ meV Å, in agreement with
weak antilocalization measurements. In the case of two occupied subbands, we observe that the intersubband
Rashba η is much weaker than the intrasubband coupling α_ν. For double wells even in the presence of strong
built-in electric fields (spontaneous and piezoelectric, crucial in GaN/AlGaN wells), we find a *seemingly*
symmetric potential configuration at which both the Rashba η and Dresselhaus Γ intersubband couplings exhibit
their highest strengths. On the other hand, we observe that the intrasubband Dresselhaus couplings β_1 and β_2
interchange their values as the gate voltage V_g varies across zero; a similar behavior, though less pronounced, is
seen for the Rashba couplings α_1 and α_2. We believe our general effective Hamiltonian for electrons in wurtzite
heterostructures put forward here, should stimulate additional theoretical works on wurtzite quantum wells,
wires, and dots with variously defined geometries and external magnetic fields.

I. INTRODUCTION

The spin-orbit interaction couples the electron spin and
its momentum. While in atomic systems this relativistic ef-
fect arises from the Coulomb potential within the atom, in
mesoscopic semiconductor heterostructures such as quantum
wells, wires, and dots, the SO interaction originates from the
interplay of the confining, doping, Hartree, and external gate
potentials. Unlike atomic systems, the SO coupling strength
in these systems can be electrically controlled, thus providing

a unique handle for the manipulation of the magnetic moment
of the electron. Spin manipulation via the SO interaction
is an important resource in spintronic devices and quantum
information processing with spin qubits [1,2].

Spin-orbit effects also underlie novel topological transport
phenomena in diverse fields of quantum condensed matter
such as topological insulators [3,4], Majorana fermions [5–7],
and Weyl semimetals [8]. Recent proposals for stretchable [9]
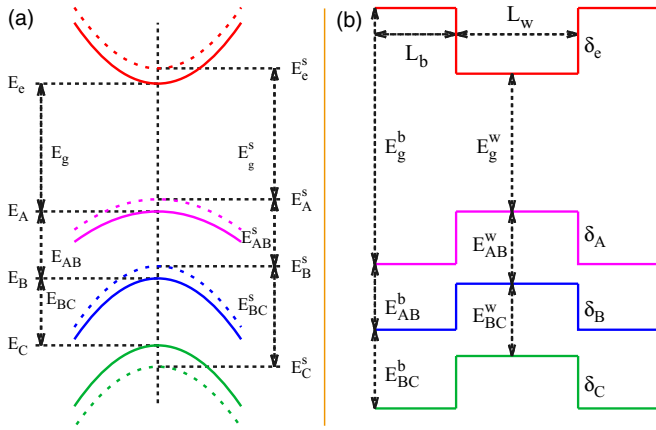spin helix [10–13] and persistent skyrmion lattice excitations

FIG. 1. (a) Schematic of the dispersion relation (CC′ basis set) of an unstrained (solid curves) and a strained (dashed curves) wurtzite semiconductor close to the Γ point ($\boldsymbol{k} = 0$). The superscript s in the band parameters indicates the strained case. (b) Potential profile of a wurtzite single well of width L_w and barriers of width L_b. The superscripts b and w stand for barrier and well, respectively. No s-p_z mixing is considered here since its effect is negligible on the band edges at the Γ point.

[14] in ordinary GaAs wells also highlight the important role of the SO in quantum wells.

So far, detailed theoretical and experimental studies on the SO coupling in semiconductors have been performed mostly in crystals with zincblende structure, including both bulk and confined systems [15,16]. It is well established by now that the structural inversion asymmetry (SIA) of wells lead to a linear-in-momentum Rashba term [17] while the bulk inversion asymmetry (BIA) of the underlying zincblende crystal lattice gives rise to linear- and cubic-in-momentum Dresselhaus terms [18] in quantum wells. Wells with two subbands also have *intersubband* Rashba- and Dresselhaus-like terms [14,15,19,20]. The interplay of the linear Rashba and Dresselhaus terms in wells gives rise to some of the interesting phenomena mentioned in the previous paragraph on zincblende matrices.

In bulk wurtzite structures, on the other hand, the presence of a hexagonal c axis along the $z||(0001)$ direction allows for a linear BIA Rashba term [21,22] (due to the s-p_z orbital mixing) in addition to a cubic BIA Dresselhaus term [23,24]. Besides terms arising from these BIA contributions, in wurtzite quantum wells a usual SIA Rashba-like term [17] is also present as we will see.

The SO coupling in wurtzite semiconductors has attracted interest both experimentally [25–34] and theoretically [23,24,35,36]. Experimentally, spin splitting energies from 0 up to 13 meV were reported in GaN-based heterostructures [25,29–31,33]. Weak antilocalization measurements provide a SO splitting parameter value ranging from 5.5 to 10.01 meV Å [26–28,30,32,34]. Compared with these measurements, the value extracted from the beating pattern of Shubnikov–de Haas oscillations is very large, around 65 meV Å, which is attributed to the structural inhomogeneity of the crystals [37].

Theoretically, Lew Yan Voon *et al.* investigated the linear Rashba-type term in bulk wurtzite semiconductors [35] and found that the linear term is mainly determined by the mixing of the s orbital of the conduction band and the p_z orbital of the valence band. This s-p_z orbital mixing was first investigated by Rashba in Ref. [38] (see also Ref. [39]). Chuang and Chang [40] investigated strained bulk wurtzite semiconductors via the $\boldsymbol{k} \cdot \boldsymbol{p}$ method and derived a Luttinger-Kohn 6×6 effective mass Hamiltonian for these systems. These authors did not include the relevant s-p_z mixing terms of Ref. [35]. Wang *et al.* studied the bulk cubic Dresselhaus SO interaction and demonstrated the existence of a zero Dresselhaus spin splitting surface in wurtzite semiconductors [23]. Fu and Wu evaluated the bulk Dresselhaus coefficient in GaN, 0.32 eV Å^3 [24], which has been experimentally verified via circular photogalvanic measurements [41]. More recently, Faria Junior *et al.* [42] investigated the bulk spin-orbit coupling effect in InP and InAs (non-nitride materials) in the wurtzite phase by combining the $\boldsymbol{k} \cdot \boldsymbol{p}$ method and *ab initio* band structure calculations.

In addition to studies on the bulk wurtzite structure, the SO coupling parameter in GaN/AlN heterostructures, around 8 meV Å, was determined by Majewski via first-principles calculations [43]. Litvinov investigated the spin splitting of GaN/AlGaAs heterostructures [36] and GaN/InGaN quantum wells with one occupied electronic subband [44]. Following the basic framework of Litvinov's formulation, Li *et al.* determined the Rashba couplings associated with two occupied electronic subbands in GaN/Al$_{0.3}$Ga$_{0.7}$N wells, with similar Rashba couplings $\alpha_1 \approx \alpha_2 \sim 0.5$ meV Å [45].

Although several investigations have been conducted so far, a comprehensive and consistent theory for the SO couplings of conduction electrons in wurtzite crystals in confined geometries is still lacking in the literature. Moreover, for the available reports on the SO coupling, the s-p_z orbital mixing, which we find is crucial in obtaining certain SO terms, was not taken into account in the Kane models used. In addition, in an earlier derivation of the effective electron Hamiltonian, the renormalization of the conduction band spinor component was not considered [36], thus leading to an energy dependent Schrödinger-type effective mass equation.

In this work we account for these missing ingredients by building on the works of Lew Yan Voon *et al.* [35] and Chuang and Chang [40] and establish a detailed systematic formulation for the electron SO interaction in wurtzite heterostructures. We then consider GaN/AlGaN wells, both single and double, involving the electron occupancy of either one or two subbands, and self-consistently determine the intrasubband (intersubband) Rashba α_ν (η), $\nu = 1, 2$, and Dresselhaus β_ν (Γ) terms. By using an external gate voltage V_g, we also discuss the electrical control of all relevant SO couplings. These SO terms are helpful to investigate spin related properties in semiconductors with wurtzite phase, especially in confined wurtzite nanostructures (wells, wires, and dots).

More specifically, we use a modified basis set ("CC′ basis"), as compared to the basis defined by Chuang and Chang [40] ("CC basis"), to construct an 8×8 Kane model, in which we account for the s-p_z orbital mixing of Lew Yan Voon *et al.* [35] (see Appendix A). The CC′ basis (Table I) is a solution of the bulk Hamiltonian at $\boldsymbol{k} = 0$ (Γ point)

with the k-independent SO coupling being partially included [Eq. (4)]. Therefore, the Kane model contains nonzero off-diagonal elements even at $k = 0$ [see Eq. (7)], implying that the diagonal elements of the Kane matrix in general do not describe the actual band edge energies, Fig. 1. We also derive the bulk Kane Hamiltonian in the "diagonal basis," in which the Kane model is diagonal at $k = 0$ (Appendix B). This helps us determine the diagonal elements (not actual band edge energies) of the Kane model in the CC′ basis as well as the corresponding "virtual" band offsets (see Table II). Having the bulk Kane model at hand, we then construct its analog for heterostructures.

We use quasidegenerate perturbation theory (Löwdin partitioning) [46] and the folding down approach [19,20] to derive an effective 2×2 electron Hamiltonian [Eq. (30)] from the 8×8 Kane model for wurtzite heterostructures. As opposed to what has been reported in the literature [36,45,47], we arrive at a *genuine* Schrödinger-type equation, i.e., an energy-independent effective Hamiltonian, since we account for the renormalization of the conduction band spinor component (Appendix C).

Our approach yields the usual linear-in-momentum Rashba term due to the SIA of the wells [Eq. (41)] and the confined BIA-induced Rashba-type SO coupling [Eq. (38)], both as functions of the s-p_z orbital mixing. Within the eight bands considered (s-conduction and p-valence bands), we also obtain the Dresselhaus coupling [Eq. (44)]. This is in contrast to systems with the zincblende structure, in which the Dresselhaus term is only present if the $k \cdot p$ interaction with remote bands, e.g., the p-conduction band, is included [48]. We also derive a general effective electron Hamiltonian containing all relevant SO terms for wurtzite nanostructures in the presence of a magnetic field and an arbitrary 3D confinement [see Eqs. (45)–(48)].

Based on our results for the SO terms, we self-consistently calculate the total spin splitting coefficient for a GaN/AlGaN single well with one occupied subband $\alpha_1^{eff} = \alpha_1 + \beta_1 \sim$ 7.16 meV Å (Figs. 2–4), in agreement with weak antilocalization measurements [28,30,34]. We determine as well the several distinct terms composing the Rashba SO coupling: the "bulk" [49], the Hartree, and the structural well contributions, and show that the strength of the SO coupling follows from the interplay of all these components, Fig. 3. For a similar calculation for zincblende quantum wells see Refs. [19,20]. Contrary to what has been predicted in an earlier work [50], we note that the bulk Rashba term dominates over all the other contributions [34,51,52]. Accordingly, the latter remains essentially constant as a function of the gate voltage V_g [37], Fig. 3(a). When the wells have two occupied subbands (higher electron density), we find that the intersubband Rashba strength η is much weaker than the intrasubband coupling α_ν, Fig. 5.

On the other hand, for GaN/AlGaN double wells (Fig. 6), interestingly, we find a *seemingly* symmetric configuration depending on the relative ratio of the Al content between the central and lateral barriers, even in the presence of the strong built-in electric field (spontaneous and piezoelectric). At this configuration, a maximal strength of the intersubband Rashba η and Dresselhaus Γ couplings occurs. In addition, by varying V_g we observe that the Dresselhaus couplings β_1 and

β_2 change dramatically and almost interchange their values. Although less pronounced, a similar behavior also holds for the Rashba couplings α_1 and α_2, see Fig. 7.

The paper is organized as follows. In Secs. II–IV we present the model and method used. Specifically, in Sec. II we review the $k \cdot p$ method and apply it to obtain an 8×8 Kane model for both unstrained and strained wurtzite wells. In Sec. III we derive a 2×2 3D SO Hamiltonian for electrons from the Kane model obtained in Sec. II. In this derivation we use both the Löwdin partitioning method and the folding down approach. By projecting the 3D Hamiltonian onto the quantum well subbands (obtained in a self-consistent way), we derive in Sec. IV an effective 2D electron Hamiltonian containing all the relevant SO terms. For concreteness, we present and discuss numerical results for GaN/AlGaN wells in Sec. V. We summarize our main findings in Sec. VI.

II. 8 × 8 KANE MODEL: BULK → HETEROSTRUCTURES

Here we first introduce the $k \cdot p$ method and then use it to derive a simple 8×8 Kane model (without contributions from remote bands) for bulk and heterostructures. These Kane models are used in Sec. III to derive 2×2 Hamiltonians for conduction electrons, in which effective spin-orbit terms arise.

A. The $k \cdot p$ method: General formulation

For an electron on a microscopic periodic potential $V(r)$, the Schrödinger equation for the periodic part $u_{\nu k}(r)$ of the Bloch function is given by [16,53,54]

$$\left[\frac{p^2}{2m_0} + V(r) + H_{so} + \frac{\hbar}{m_0} k \cdot \pi \right] u_{\nu k}(r)$$
$$= \left(E_\nu(k) - \frac{\hbar^2 k^2}{2m_0} \right) u_{\nu k}(r), \quad (1)$$

where m_0 is the bare electron mass, ν is a band index for each wave vector k, p is the momentum operator, and

$$\pi = p + \frac{\hbar}{4m_0 c^2} \sigma \times \nabla V(r), \quad (2)$$

with $\sigma = (\sigma_x, \sigma_y, \sigma_z)$ being the Pauli matrices. The spin-orbit coupling appears in Eq. (1) as the $k = 0$ term

$$H_{so} = \frac{\hbar}{4m_0^2 c^2} \nabla V(r) \times p \cdot \sigma, \quad (3)$$

and the k-linear term $\frac{\hbar}{m_0} k \cdot \pi$.

The Hamiltonian above considers an unstrained crystal. For a finite strain, one must add the strain related couplings H_{strain} to Eq. (1) [55,56]. We will discuss the strain tensor and its effects in Sec. II B 2.

To solve Eq. (1) in the vicinity of the Γ point ($k \approx 0$) within the $k \cdot p$ approach, one must define a basis set $\{u_{\nu 0}(r)\}$ at $k = 0$ to expand $u_{\nu k}(r)$. This choice of basis set is in principle not unique and leads to different representations of the Kane model [16,54]. Ideally, one would prefer to work on a basis set that diagonalizes Eq. (1) at $k = 0$, as it is commonly done for zincblende structures. However, it is often

more interesting to use a basis defined by the irreducible representations (IRREPs) of the crystal's group, which is not always diagonal at $k = 0$. This is the case for the basis set defined by Chuang and Chang [40].

B. 8 × 8 Kane model: Bulk

In this subsection we use the CC′ basis [35]—a modified basis set that incorporates previously neglected effects of the s-p_z coupling [40] (see Appendix A for more details)—defined in Table I, to construct our 8 × 8 Kane Hamiltonian.

1. CC′ basis: Unstrained case

Our basis set is defined by splitting the total Hamiltonian in Eq. (1) as $H = H_0^{CC'} + W^{CC'}(k)$, with

$$H_0^{CC'} = \frac{p^2}{2m_0} + V(r) + H_{soz}, \tag{4}$$

$$W^{CC'}(k) = \frac{\hbar}{m_0} k \cdot \pi + H_{sox} + H_{soy}, \tag{5}$$

$$H_{soj} = \frac{\hbar}{4m_0^2 c^2} [\nabla V(r) \times p]_j \, \sigma_j, \tag{6}$$

where $j = \{x, y, z\}$ labels the spin components of H_{so}. The chosen CC′ basis is composed by the eigenstates that diagonalize $H_0^{CC'}$, which includes only the z component (H_{soz}) of the $k = 0$ spin-orbit interaction. Therefore, our Hamiltonian will not be diagonal at $k = 0$, since the perturbation $W^{CC'}(k)$ contains the k-independent H_{sox} and H_{soy} terms.

Wurtzite crystals comprise two interpenetrating hexagonal lattices that transform according to the space group $P6_3mc$ (C_{6v}^4), yielding the C_{6v} point group at Γ ($k = 0$) [57]. Hence,

TABLE I. CC′ basis functions $u_{\nu' 0}^{CC'}(r) \equiv u_{\nu' 0}(r) \equiv \langle r|\nu'\rangle$, with $\nu' = 1, 2, \ldots, 8$. The states $|S'\rangle$ and $|Z'\rangle$ transform like scalars and $\{|X\rangle, |Y\rangle\}$ transform like vectors. The corresponding doubly degenerate band edges (at the Γ point) are denoted by E_e (conduction) and E_A, E_B, E_C (valence) bands, respectively. The s-p_z mixed orbitals are $|S'\rangle = q_s|S\rangle + q_z|Z\rangle$, and $|Z'\rangle = q_s|Z\rangle - q_z|S\rangle$, with $|q_s|^2 + |q_z|^2 = 1$ and $q_z \ll 1$ (Appendix A).

	ν'	$|\nu'\rangle$	C_{6v} IRREP
e	1	$|iS'\uparrow\rangle$	Γ_1
e	2	$|iS'\downarrow\rangle$	Γ_1
A	3	$-\frac{1}{\sqrt{2}}|X + iY\uparrow\rangle$	Γ_5
A	4	$+\frac{1}{\sqrt{2}}|X - iY\downarrow\rangle$	Γ_5
B	5	$+\frac{1}{\sqrt{2}}|X - iY\uparrow\rangle$	Γ_5
B	6	$-\frac{1}{\sqrt{2}}|X + iY\downarrow\rangle$	Γ_5
C	7	$|Z'\uparrow\rangle$	Γ_1
C	8	$|Z'\downarrow\rangle$	Γ_1

the solutions of $H_0^{CC'}$ are given by single-group states belonging to the Γ_1 (S and Z) [58] and Γ_5 ($\{X, Y\}$) IRREPs of C_{6v}, with well defined spin ($\uparrow$ and $\downarrow$) along the z direction. Note that differently from zincblende crystals, the z direction in the wurtzite unit cell is nonequivalent to the x and y directions. This allows for an s-p_z mixing [35,38,39], thus leading to the hybridized S' and Z' orbitals shown in Table I.

Using the CC′ basis listed in Table I, we can now build the bulk 8 × 8 Kane Hamiltonian $H_{8\times8}^{CC'}$. We find [62] (see Appendix A 4)

$$H_{8\times8}^{CC'} = \frac{p^2}{2m_0} + \begin{pmatrix} 0 & 0 & -\frac{1}{\sqrt{2}}P_2 k_+ & 0 & \frac{1}{\sqrt{2}}P_2 k_- & -i\sqrt{2}\Delta_{sz} & P_1 k_z & 0 \\ 0 & 0 & 0 & \frac{1}{\sqrt{2}}P_2 k_- & -i\sqrt{2}\Delta_{sz} & -\frac{1}{\sqrt{2}}P_2 k_+ & 0 & P_1 k_z \\ -\frac{1}{\sqrt{2}}P_2 k_- & 0 & -E_g^{CC'} & 0 & 0 & 0 & 0 & 0 \\ 0 & \frac{1}{\sqrt{2}}P_2 k_+ & 0 & -E_g^{CC'} & 0 & 0 & 0 & 0 \\ \frac{1}{\sqrt{2}}P_2 k_+ & i\sqrt{2}\Delta_{sz} & 0 & 0 & -E_g^{CC'} - E_{AB} & 0 & 0 & \sqrt{2}\Delta_3 \\ i\sqrt{2}\Delta_{sz} & -\frac{1}{\sqrt{2}}P_2 k_- & 0 & 0 & 0 & -E_g^{CC'} - E_{AB} & \sqrt{2}\Delta_3 & 0 \\ P_1 k_z & 0 & 0 & 0 & 0 & \sqrt{2}\Delta_3 & -E_g^{CC'} - E_{AC} & 0 \\ 0 & P_1 k_z & 0 & 0 & \sqrt{2}\Delta_3 & 0 & 0 & -E_g^{CC'} - E_{AC} \end{pmatrix}. \tag{7}$$

The nonzero spin-orbit matrix element Δ_{sz} was neglected in the original work by Chuang and Chang [40], see Appendix A for details on the origin of this term. However, this term is allowed by symmetry, i.e., by the mixing of the orbitals "s" and "p_z." Namely, this spin-orbit coupling Δ_{sz} reads

$$\Delta_{sz} = \frac{\hbar^2}{4m_0^2 c^2} \langle Y| \frac{\partial V}{\partial y} \frac{\partial}{\partial z} - \frac{\partial V}{\partial z} \frac{\partial}{\partial y} |S'\rangle. \tag{8}$$

Even though this term has a negligible effect on the band edges at $k = 0$, it is crucial in obtaining the relevant SO terms at $k \neq 0$.

The diagonal matrix elements in Eq. (7) are the eigenenergies of $H_0^{CC'}$ [see Eq. (4)]; here we set $E_e \equiv 0$ (energy reference), $E_A = -E_g^{CC'}$, $E_B = -E_g^{CC'} - E_{AB}$, and $E_C = -E_g^{CC'} - E_{AC}$, with the subscripts e denoting the lowest conduction band and A, B, and C the topmost three valence bands, respectively. The term $E_g^{CC'} \approx E_g$ corresponds to the band gap

(see discussion below). The energy differences between the valence band edges are given by

$$E_{AB} = 2\Delta_2, \quad E_{AC} = \Delta_1 + \Delta_2, \tag{9}$$

where $\Delta_1 \equiv \Delta_{\text{cr}}$ is the crystal-field splitting energy, and Δ_2 and Δ_3 are two SO split-off energy parameters, which read

$$\Delta_2 = -\frac{\hbar^2}{4m_0^2 c^2} \langle Y | \frac{\partial V}{\partial x}\frac{\partial}{\partial y} - \frac{\partial V}{\partial y}\frac{\partial}{\partial x} | X \rangle, \tag{10}$$

$$\Delta_3 = \frac{\hbar^2}{4m_0^2 c^2} \langle Y | \frac{\partial V}{\partial y}\frac{\partial}{\partial z} - \frac{\partial V}{\partial z}\frac{\partial}{\partial y} | Z' \rangle. \tag{11}$$

These are commonly assumed to be related by $\Delta_2 = \Delta_3 \equiv \Delta_{\text{so}}/3$ [63], following the quasicubic approximation [54]. The off-diagonal $\boldsymbol{k}$-linear terms are defined by Kane parameters $P_1 = -(i\hbar/m_0)\langle S'|p_z|Z'\rangle$ and $P_2 = -(i\hbar/m_0)\langle S'|p_x|X\rangle = -(i\hbar/m_0)\langle S'|p_y|Y\rangle$, with $k_\pm = k_x \pm ik_y$.

The Hamiltonian in Eq. (7) is well defined in terms of the matrix elements shown above. Note, however, that the diagonal matrix elements do not correspond to the real band edges, since $H_{8\times8}^{\text{CC}'}$ is not diagonal at $k = 0$. Nevertheless, we can safely use $E_g^{\text{CC}'} \approx E_g$ (real band gap) since (i) Eq. (7) shows that the topmost valence band A does not couple to other bands at $\boldsymbol{k} = 0$, and (ii) the Δ_{sz} coupling between the conduction and valence bands leads to a negligible second-order correction for the conduction band at $\boldsymbol{k} = 0$, i.e., $E_g = E_g^{\text{CC}'} - 2\Delta_{\text{sz}}^2/(E_g^{\text{CC}'} + E_{AB}) \approx E_g^{\text{CC}'}$.

2. CC′ basis: Strained case

The application of an external stress on a bulk semiconductor leads to a shift of the energy levels and/or a splitting of the heavy-light holes degeneracy [55]. We discuss now how strain effects change the band edges of the $\boldsymbol{k} \cdot \boldsymbol{p}$ Hamiltonian in Eq. (7).

We restrict ourselves to the case of biaxial strain, i.e.,

$$\begin{aligned} \varepsilon_{xx} &= \varepsilon_{yy} \neq \varepsilon_{zz}, \\ \varepsilon_{xy} &= \varepsilon_{yz} = \varepsilon_{zx} = 0, \end{aligned} \tag{12}$$

where ε_{ij} ($i, j = x, y, z$) is the strain tensor. Notice that strain appearing in heterostructures is in general caused by a lattice mismatch at the interfaces. For a strained-layer wurtzite crystal pseudomorphically grown along the [0001] crystallographic direction, the components of the strain tensor assume the following values: $\varepsilon_{xx} = \varepsilon_{yy} = (a_s - a)/a$ and $\varepsilon_{zz} = -2C_{13}\varepsilon_{xx}/C_{33}$, where a_s is the lattice constant of the substrate and a of the epitaxy layer. The parameters C_{13} and C_{33} are the elastic stiffness constants [40,64–66].

The conduction band edge has a hydrostatic energy shift given by $\Delta E_e = a_{c_1}\varepsilon_{zz} + a_{c_2}(\varepsilon_{xx} + \varepsilon_{yy})$, with $a_{c_1(c_2)}$ the conduction band deformation potential. The topmost A valence band edge shifts according to $\Delta E_A = S_1 + S_2$, where S_1 and S_2 are written as $S_1 = D_1\varepsilon_{zz} + D_2(\varepsilon_{xx} + \varepsilon_{yy})$ and $S_2 = D_3\varepsilon_{zz} + D_4(\varepsilon_{xx} + \varepsilon_{yy})$, with D_{1-4} the valence band deformation potentials [40,67]. Therefore, the band gap variation, i.e., $\Delta E_g = E_g^s - E_g$, is given by $\Delta E_e - \Delta E_A$, with the superscript "s" denoting parameters in the strained case. The energy

differences between valence bands read

$$E_{AB}^s = E_{AB} = 2\Delta_2, \tag{13}$$

$$E_{AC}^s = E_{AC} + S_2 = \Delta_1 + \Delta_2 + S_2, \tag{14}$$

where one can explicitly see the band edge corrections due to the deformation potentials [cf. Eqs. (9), (13), and (14)].

In Fig. 1(a) we show the diagonal matrix elements for both cases: unstrained (solid curves) and strained (dashed curves). Here the only effect caused by strain is a shift in the band edges; one can then straightforwardly write down the corresponding Kane Hamiltonian by simply replacing E_g, E_{AB}, and E_{AC} in Eq. (7) by E_g^s, E_{AB}^s, and E_{AC}^s, respectively.

3. Some remarks

The Kane model in Eq. (7) was constructed including only the lowest conduction [58] and top valence bands (see Table I). This model only provides a good description of the electronic states in the conduction band. In order to properly describe holes, especially heavy and light holes, it is necessary to include additional bands [54]. Nevertheless, here we are just interested in the conduction band. From Eqs. (23) and (24), for instance, we can calculate the longitudinal and transversal electronic effective masses, respectively, which, as we shall see in Sec. V, are in excellent agreement with experimental results.

We also derive a Kane Hamiltonian using the "diagonal basis," in which the 8×8 matrix is diagonal at $\mathbf{k} = 0$ (see Appendix B). This helps us determine the diagonal elements (not actual band edge energies) of the Kane model in the CC′ basis, as well as the corresponding "virtual" band offsets (see Table II) to correctly describe heterostructures. Note, though, that the diagonal basis has a direct dependence on the band parameters.

C. 8 × 8 Kane model: Heterostructures

We shall focus now on the Kane model for wurtzite heterostructures, more specifically quantum wells grown along the $z||(0001)$ direction (c axis), for which experimental data are available. Later on, we show a general formulation valid for wells, as well as wires and dots (see Sec. III C).

Due to the different band edges at $\boldsymbol{k} = 0$ for different materials, a sharp jump of the bands (offsets) happens at the interfaces, which introduces position-dependent potentials representing the different layers. For simplicity, we refer here to the unstrained case; the generalization to the strained case is straightforward (see Sec. II B 2).

The Hamiltonian for wells looks exactly the same as that in Eq. (7), except that now one has to replace $k_z \rightarrow -i(\partial/\partial z)$, and introduce in the diagonal z-dependent potentials to account for the band offsets. Note that the diagonal basis functions depend on the band parameters (see Table IV in Appendix B), and hence, have different values on the well and on the barriers. This may lead to unnecessary complications in practice [68]. For convenience, we only consider the 8×8 Kane model for wells written in the CC′ basis. We emphasize that, strictly speaking, even in the CC′ basis set, the basis functions are z dependent, as the periodic part of the Bloch functions, i.e., S, X, Y, and Z, see Table I, can be different

for the several layers. Here we neglect this difference, as it is usually done for zincblende heterostructures [68,69].

1. Unstrained quantum wells

Let us first analyze the z-dependent structural potential added to the diagonal part of Hamiltonian (7), for both the conduction and valence bands. From Fig. 1(b), where we schematically show the band offsets, we can straightforwardly obtain

$$V_{w-e}(z) = \delta_e h_w(z), \quad V_{w-i}(z) = -\delta_i h_w(z), \quad i \in \{A, B, C\},$$
(15)

where $h_w(z) = \Theta(z - \frac{L_w}{2}) + \Theta(-z - \frac{L_w}{2})$ describes a dimensionless square well profile, with $\Theta(z)$ the Heaviside function. In this expression, the center of the well has been taken as the origin in the z direction ($z = 0$).

Once again, in addition to the z-dependent potentials in Eq. (15), the off-diagonal elements Δ_3, Δ_{sz}, and the Kane parameters P_1 and P_2 should be z dependent, since in principle they may have distinct values in different layers. In most wurtzite materials, though, they have very similar values [66], and from now on, we use them as z-independent parameters.

The discussion above on the Kane Hamiltonian for a quantum well is based on the single-electron picture, in which the electrons experience only the structural potential of the well. Below we focus on modulation doped quantum wells in the Hartree approximation. In this case, besides the structural well potential, the doping (from dopants) potential, the pure electron Hartree (from electrons) potential, as well as the external gate potential also contribute to the total electron potential.

2. Strained quantum wells

For strained wurtzite heterostructures, an internal potential (built-in electric field), due to the strain-induced piezoelectric polarization and/or spontaneous polarization, usually plays a significant role as well [70]. To calculate the built-in fields, two types of boundary conditions are usually used: (i) periodic boundary conditions, i.e., the potentials of the external surfaces are equal, and (ii) neutral external surfaces [71,72]. The corresponding expressions for the electric fields E_w (well) and E_b (barriers) in both cases are given by

(i) periodic boundary conditions

$$E_w = \frac{2L_b(P_b - P_w)}{\epsilon_0 \epsilon_r (L_w + 2L_b)}, \quad E_b = E_w + \frac{P_w - P_b}{\epsilon_0 \epsilon_r}, \quad (16)$$

(ii) neutral external surfaces

$$E_w = \frac{P_b - P_w}{\epsilon_0 \epsilon_r}, \quad E_b = 0, \quad (17)$$

where ϵ_0 is the vacuum permittivity and P_w and P_b are the polarization fields (spontaneous and piezoelectric) appearing in the well and barriers, respectively. Here we have assumed a uniform dielectric constant ϵ_r throughout the system. Note that, as the width of the barriers L_b goes to infinity, the two types of boundary conditions become equivalent.

The direction and magnitude of the spontaneous polarization along the c axis of a wurtzite crystal can be determined

experimentally [70,73,74]. On the other hand, the magnitude of the piezoelectric polarization reads

$$P = 2\frac{a_s - a}{a}\left(e_{31} - e_{33}\frac{C_{13}}{C_{33}}\right), \quad (18)$$

where e_{31} and e_{33} are piezoelectric coefficients. Both polarizations are calculated for the well and also for the barrier.

3. Total potential

The total self-consistent conduction and valence band potentials $V_e(z)$ and $V_i(z)$, $i \in \{A, B, C\}$, respectively, in strained wurtzite quantum wells are given by

$$V_e(z) = V_H(z) + V_{w-e}(z), \quad V_i(z) = V_H(z) + V_{w-i}(z), \quad (19)$$

with V_H the Hartree potential, which also has several contributions, namely,

$$V_H(z) = V_{\text{elect}}(z) + V_d(z) + V_{\text{int}}(z) + V_g(z), \quad (20)$$

where V_{elect} is the pure electron Hartree potential, V_d is the doping potential, V_{int} is the internal potential (due to the built-in electric field), and V_g is the external gate potential (see Appendix E for details).

III. EFFECTIVE 2 × 2 CONDUCTION HAMILTONIAN (3D)

Based on the 8×8 Kane model for wurzite structures discussed in the last section, we now derive an effective 2×2 Hamiltonain for the conduction band electrons in bulk and heterostructures. To this end we can either use the Löwdin partitioning method, discussed in detail in Refs. [16,46], or the folding down approach, shown in Appendix C. We use both approaches and obtain the same result. In particular, we present a very general effective Hamiltonian for electrons valid, in quantum wells, wires, and dots with arbitrary potentials and magnetic fields.

A. Bulk: The appearance of the BIA Rashba and the BIA Dresselhaus terms

From the 8×8 Kane model in Eq. (7), we obtain (up to third order in the energy denominator) the effective 2×2 bulk Hamiltonian for the conduction-band electrons

$$\mathcal{H}_{\text{bulk}} = \mathcal{H}_0 + \mathcal{H}_{\text{bulk}}^R + \mathcal{H}_{\text{bulk}}^D, \quad (21)$$

where

$$\mathcal{H}_0 = \frac{\hbar^2 k_z^2}{2m_\perp^2} + \frac{\hbar^2 k_\parallel^2}{2m_\parallel^2} \quad (22)$$

is the kinetic Hamiltonian, with $k_\parallel^2 = k_x^2 + k_y^2$ and effective masses given by

$$\frac{1}{m_\perp} = \frac{1}{m_0} + \frac{2P_1^2}{\hbar^2}\frac{1}{E_g + \Delta_1 + \Delta_2}, \quad (23)$$

$$\frac{1}{m_\parallel} = \frac{1}{m_0} + \frac{P_2^2}{\hbar^2}\left(\frac{1}{E_g} + \frac{1}{E_g + 2\Delta_2}\right). \quad (24)$$

The last two contributions in Eq. (21) correspond, respectively, to the k-linear BIA Rashba Hamiltonian

$$\mathcal{H}_{\text{bulk}}^R = \alpha_{\text{bulk}}^{\text{BIA}}(\sigma_x k_y - \sigma_y k_x), \tag{25}$$

and the k-cubic BIA Dresselhaus Hamiltonian [23], which in wurtzite crystals has the same functional form as the Rashba term, i.e.,

$$\mathcal{H}_{\text{bulk}}^D = \gamma(b k_z^2 - k_\parallel^2)(\sigma_x k_y - \sigma_y k_x). \tag{26}$$

See Appendix A 2 b for a derivation of Eq. (26) using the theory of invariants. Within our model, the SO parameters $\alpha_{\text{bulk}}^{\text{BIA}}$, γ, and b are determined by the bulk quantities of the material and read

$$\alpha_{\text{bulk}}^{\text{BIA}} = \frac{2P_2 \Delta_{\text{sz}}}{(E_g + 2\Delta_2)} + \frac{4P_2 \Delta_3^2 \Delta_{\text{sz}}}{(E_g + 2\Delta_2)^2(E_g + \Delta_1 + \Delta_2)}$$
$$- \frac{8P_2 \Delta_{\text{sz}}^3}{(E_g + 2\Delta_2)^3}, \tag{27}$$

$$\gamma = -\frac{P_2^3 \Delta_{\text{sz}}}{E_g + E_{AB}}\left[\frac{1}{E_g^2} + \frac{2}{(E_g + E_{AB})^2} + \frac{1}{E_g(E_g + E_{AB})}\right], \tag{28}$$

$$b = -\frac{2P_1^2 P_2 \Delta_{\text{sz}}}{\gamma_1(E_g + E_{AB})(E_g + E_{AC})}\left(\frac{1}{E_g + E_{AC}} + \frac{1}{E_g + E_{AB}}\right). \tag{29}$$

Note indeed that the couplings above are proportional to the spin-orbit parameter Δ_{sz}, which is finite only due to the broken cubic symmetry of the wurtzite crystal that allows for the s-p_z orbital mixing. It is important to emphasize that the cubic form of our $\mathcal{H}_{\text{bulk}}^D$ as derived within our 8×8 Kane model is correct [23]; note, however, that the bulk Dresselhaus parameters γ and b, in Eqs. (28) and (29) respectively, are too small and are treated phenomenologically in our simulations later on. Interestingly, the expression for $\alpha_{\text{bulk}}^{\text{BIA}}$ in Eq. (27), derived within our model, gives values in agreement with experiments [34].

B. Quantum well: SIA Rashba, BIA Rashba, and BIA Dresselhaus terms

Using Eq. (7), with $k_z \to -i\partial/\partial_z$, and the conduction and valence-band potentials of Eq. (19) added to its diagonal, we derive the following effective 2×2 Hamiltonian for wurtzite quantum wells

$$\mathcal{H}^{\text{3D}} = \mathcal{H}_{\text{qw}} + \mathcal{H}_{\text{so}}^R + \mathcal{H}_{\text{so}}^D, \tag{30}$$

where the first contribution is spin independent and the last two terms correspond to the Rashba and Dresselhaus SO interactions, respectively. The spin independent part of Eq. (30) is given by

$$\mathcal{H}_{\text{qw}}(z) = -\frac{\hbar^2}{2}\frac{d}{dz}\frac{1}{m_\perp(z)}\frac{d}{dz} + \frac{\hbar^2 k_\parallel^2}{2m_\parallel(z)} + V_{\text{eff}}(z) + V_e(z), \tag{31}$$

with $m_\perp$ and $m_\parallel$ the longitudinal and transversal effective masses, respectively,

$$\frac{1}{m_\perp(z)} = \frac{1}{m_0} + \frac{2P_1^2}{\hbar^2}\left[\frac{1}{E_g + \Delta_1 + \Delta_2} - \frac{V_e(z) - V_C(z)}{(E_g + \Delta_1 + \Delta_2)^2}\right], \tag{32}$$

$$\frac{1}{m_\parallel(z)} = \frac{1}{m_0} + \frac{P_2^2}{\hbar^2}\left[\frac{1}{E_g} + \frac{1}{E_g + 2\Delta_2}\right.$$
$$\left. - \frac{V_e(z) - V_A(z)}{E_g^2} - \frac{V_e(z) - V_B(z)}{(E_g + 2\Delta_2)^2}\right]. \tag{33}$$

The extra effective potential $V_{\text{eff}} = V_D + V_s$ includes the Darwin term V_D and an s-p_z mixing-induced contribution V_s. The corresponding expressions read

$$V_D(z) = \frac{P_1^2}{2(E_g + \Delta_1 + \Delta_2)^2}\frac{d^2 V_e(z)}{dz^2}, \tag{34}$$

$$V_s(z) = \frac{2\Delta_{\text{sz}}^2}{E_g + 2\Delta_2} - \frac{2\Delta_{\text{sz}}^2[V_e(z) - V_B(z)]}{(E_g + 2\Delta_2)^2}. \tag{35}$$

The spin-dependent Rashba SO Hamiltonian reads

$$\mathcal{H}_{\text{so}}^R = \eta(z)(\sigma_x k_y - \sigma_y k_x), \tag{36}$$

where the coupling parameter $\eta(z)$ has contributions from both the bulk and structural inversion asymmetries

$$\eta(z) = \eta_{\text{BIA}}(z) + \eta_{\text{SIA}}(z). \tag{37}$$

The bulk Rashba contribution is given by

$$\eta_{\text{BIA}}(z) = \frac{2P_2 \Delta_{\text{sz}}}{E_g + 2\Delta_2}\left[1 + \frac{4\Delta_3^2}{(E_g + 2\Delta_2)(E_g + \Delta_1 + \Delta_2)}\right.$$
$$\left. - \frac{8\Delta_{\text{sz}}^2}{(E_g + 2\Delta_2)^2} - \frac{V_e(z) - V_B(z)}{E_g + 2\Delta_2}\right]. \tag{38}$$

Note that $\eta_{\text{BIA}}(z)$ takes different values in each layer (well and barrier), i.e., for $|z| < L_w/2$,

$$\eta_{\text{BIA}}(z) \equiv \eta_{\text{BIA}}(\text{well}) = \alpha_{\text{bulk}}^{\text{BIA}}, \tag{39}$$

see Eq. (27), and for $|z| > L_w/2$,

$$\eta_{\text{BIA}}(z) \equiv \eta_{\text{BIA}}(\text{barrier}) = \alpha_{\text{bulk}}^{\text{BIA}} - (\delta_e + \delta_B)\frac{2P_2 \Delta_{\text{sz}}}{(E_g + 2\Delta_2)^2}, \tag{40}$$

see [75]. We should emphasize that there is no analog of such a contribution to the SO interaction in zincblende systems, in which the s-p_z mixing is not allowed by symmetry.

The SIA term, on the other hand, has contributions from the Hartree and structural potentials

$$\eta_{\text{SIA}}(z) = \eta_H \frac{dV_H(z)}{dz} + \eta_w \frac{dV_{w-e}(z)}{dz}, \tag{41}$$

where

$$\eta_H = \frac{P_1 P_2 \Delta_3}{(E_g + 2\Delta_2)(E_g + \Delta_1 + \Delta_2)}$$
$$\times \left(\frac{1}{E_g + 2\Delta_2} + \frac{1}{E_g + \Delta_1 + \Delta_2}\right) \tag{42}$$

and

$$\eta_w = -\frac{P_1 P_2 \Delta_3}{(E_g + 2\Delta_2)(E_g + \Delta_1 + \Delta_2)}$$
$$\times \left(\frac{\delta_C/\delta_e}{E_g + 2\Delta_2} + \frac{\delta_B/\delta_e}{E_g + \Delta_1 + \Delta_2} \right). \quad (43)$$

In Sec. IV we show that $\eta_{\text{SIA}}(z)$ in Eq. (41) corresponds to the usual Rashba coupling in 2DEGs.

The expressions shown above for the Rashba coupling do not account for possible $\mathbf{k} \cdot \mathbf{p}$ terms within the valence band subspace. In wurtzite structures these terms are allowed by point-group symmetry arguments [76,77]. In zincblende systems, they are also allowed by symmetry, but were shown to be zero by Cardona *et al.* [48]. In Appendix D we obtain the corresponding expression of H_v (valence band subspace) for wurtzite quantum wells including the $\mathbf{k} \cdot \mathbf{p}$ interaction within the valence bands, characterized by the parameter $Q = -(i\hbar/m_0)\langle Z'|p_x|X\rangle = (i\hbar/m_0)\langle Z'|p_y|Y\rangle$. The additional terms in the 2×2 electron Hamiltonian are also derived. We show that their contributions are negligible to the Rashba SO coupling.

The Dresselhaus SO Hamiltonian for the wurtzite quantum well in Eq. (30) reads

$$\mathcal{H}_{\text{so}}^D = \gamma \left(-b\frac{d^2}{dz^2} - k_\parallel^2 \right)(\sigma_x k_y - \sigma_y k_x), \quad (44)$$

in which γ and b are given in Eqs. (28) and (29), respectively. For more details, see Appendix A 2 a, in which we derive Eq. (44) using the theory of invariants. For completeness, in Appendix D we derive the Dresselhaus Hamiltonian accounting for the $\mathbf{k} \cdot \mathbf{p}$ coupling within the valence bands. As it turns out, these new terms also contribute negligibly to the Dresselhaus SO coupling; the calculated γ and b of Eqs. (D5) and (D10) are too small as compared to an earlier semiempirical calculation [24] and experiment [41]. Later on in our simulations, we use γ and b in Eq. (44) as semiempirical constants taken from Refs. [23,24].

C. General expression

For completeness we present below the general effective Schrödinger equation for electrons in wurtzite heterostructures with an arbitrary confining potential and external magnetic field. More specifically, our general result is valid for quantum wells, wires, and dots (cf. Eq. (6.26) in Ref. [16] for zincblende heterostructures).

The total 2×2 Hamiltonian reads

$$H_{\text{eff}} = H_0 + H_{\text{B}} + H_{\text{so}}, \quad (45)$$

in which H_0 is spin independent, H_{B} corresponds to the Zeeman term, and H_{so} is the SO coupling. The expression for H_0 is given by

$$H_0 = \frac{\hbar^2}{2}\left[\mathbf{k}_\parallel \frac{1}{m_\parallel(\mathbf{r})}\mathbf{k}_\parallel + k_z \frac{1}{m_\perp(\mathbf{r})}k_z \right] + V_e(\mathbf{r}) + \frac{2\Delta_{\text{sz}}^2}{E_g + 2\Delta_2}\left[1 - \frac{V_e(\mathbf{r}) - V_B(\mathbf{r})}{E_g + 2\Delta_2} \right]$$
$$+ \frac{P_1^2}{(E_g + \Delta_1 + \Delta_2)^2}\frac{\partial^2 V_e(\mathbf{r})}{\partial z^2} + \left[\frac{P_2^2}{E_g^2} + \frac{P_2^2}{(E_g + 2\Delta_2)^2} \right]\nabla_\parallel^2 V_e(\mathbf{r}), \quad (46)$$

where the out-of-plane and in-plane effective masses, which now that depend on $\mathbf{r}$, are given by Eqs. (32) and (33), respectively. The last two terms in Eq. (46) are equivalent to the Darwin term in the Pauli equation [78]. The Zeeman term can be written as

$$H_{\text{B}} = -\frac{e}{\hbar}\frac{P_1 P_2 \Delta_3}{(E_g + 2\Delta_2)(E_g + \Delta_1 + \Delta_2)}\left(1 - \frac{V_e(\mathbf{r}) - V_B(\mathbf{r})}{E_g + 2\Delta_2} + \frac{V_e(\mathbf{r}) - V_C(\mathbf{r})}{E_g + \Delta_1 + \Delta_2} \right)(\sigma_x B_x + \sigma_y B_y)$$
$$+ \frac{e}{\hbar}\frac{P_2^2}{2}\left(-\frac{V_A(\mathbf{r})}{E_g^2} + \frac{V_B(\mathbf{r})}{(E_g + 2\Delta_2)^2} \right)\sigma_z B_z, \quad (47)$$

where $\mathbf{B} = \sum_{i=x,y,z} B_i \hat{\mathbf{i}}$ is the applied magnetic field. The SO Hamiltonian, up to first order in $k_\parallel$, reads

$$H_{\text{so}} = \left(\frac{2P_2\Delta_{\text{sz}}}{E_g + 2\Delta_2} + \frac{4P_2\Delta_3^2\Delta_{\text{sz}}}{(E_g + 2\Delta_2)^2(E_g + \Delta_1 + \Delta_2)} - \frac{8P_2\Delta_{\text{sz}}^3}{(E_g + 2\Delta_2)^3} \right)(\sigma_x k_y - \sigma_y k_x) - \frac{P_2\Delta_{\text{sz}}}{(E_g + 2\Delta_2)^2}\{\sigma_x k_y - \sigma_y k_x, V_e(\mathbf{r}) - V_B(\mathbf{r})\}$$
$$+ \frac{P_2^2}{2E_g^2}[\mathbf{k} \times \nabla V_A(\mathbf{r})]_z \sigma_z - \frac{P_2^2}{2(E_g + 2\Delta_2)^2}[\mathbf{k} \times \nabla V_B(\mathbf{r})]_z \sigma_z + \frac{P_1 P_2 \Delta_3}{(E_g + 2\Delta_2)^2(E_g + \Delta_1 + \Delta_2)}\boldsymbol{\sigma}_\parallel \cdot [\mathbf{k} \times \nabla V_B(\mathbf{r})]_\parallel$$
$$+ \frac{P_1 P_2 \Delta_3}{(E_g + 2\Delta_2)(E_g + \Delta_1 + \Delta_2)^2}\boldsymbol{\sigma}_\parallel \cdot [\mathbf{k} \times \nabla V_C(\mathbf{r})]_\parallel + \frac{P_2\Delta_{\text{sz}}}{(E_g + 2\Delta_2)^3}\left\{ \sigma_x k_y - \sigma_y k_x, V_e^2(\mathbf{r}) + V_B^2(\mathbf{r}) \right\}$$
$$- \frac{P_2\Delta_{\text{sz}}}{(E_g + 2\Delta_2)^3}[\{V_e(\mathbf{r}), (\sigma_x k_y - \sigma_y k_x)V_B(\mathbf{r})\} + \{V_B(\mathbf{r}), (\sigma_x k_y - \sigma_y k_x)V_e(\mathbf{r})\}], \quad (48)$$

with $\mathbf{k}$ the kinetic momentum, i.e., $\hbar\mathbf{k} = -i\hbar\nabla + e\mathbf{A}$, $\mathbf{B} = \nabla \times \mathbf{A}$ (real external field), which should be distinguished from the canonical momentum $\hbar\mathbf{k} = -i\hbar\nabla$. The bracket $\{\cdot, \cdot\}$ stands for the anticommutator.

The general Hamiltonian in Eq. (45) is one of the main results of the present paper. We must point out a major difference between the latter and the effective model for zincblende structures [16]: the nonequivalence between the z direction with respect to x and y allows for the s-p_z hybridization, which then leads to the emergence of additional terms when spin orbit is considered [see coefficients $\propto \Delta_{sz}$ in Eqs. (46) and (48)].

From the expressions above, it is quite simple to see this nonequivalence between z and x, y. For the sake of simplicity, let us focus on the bulk case. In addition to having different effective masses in the longitudinal and transversal directions [see Eqs. (23) and (24), respectively], Eq. (47) reveals an anisotropy in the effective g factor, there is no z component. This feature, as well as the analysis of the extra terms mentioned above, will be addressed elsewhere.

Our general Hamiltonian can be used to study a variety of heterostructures. Note that, apart from the Dresselhaus term (not included in the derivation above), Eqs. (21) and (30) are particular cases of Eq. (45). Next we focus on one- and two-subband quantum wells, for which we can write down an effective Hamiltonian and self-consistently determine all the relevant SO couplings.

IV. EFFECTIVE 4 × 4 HAMILTONIAN

From the 3D Hamiltonian of Sec. III B, we can derive an effective low-energy quasi-2D model. More specifically, here we obtain a model Hamiltonian for quantum wells with one and two subbands.

Our approach consists first in self-consistently determining the spin-degenerate eigenvalues $\mathcal{E}_{\boldsymbol{k}_\parallel \nu} = \mathcal{E}_\nu + \hbar^2 k_\parallel^2 / 2 m_\parallel$ and corresponding eigenspinors $|\boldsymbol{k}_\parallel \nu \sigma\rangle = |\boldsymbol{k}_\parallel \nu\rangle \otimes |\sigma\rangle$, $\langle \boldsymbol{r}|\boldsymbol{k}_\parallel \nu\rangle = e^{i\boldsymbol{k}_\parallel \cdot \boldsymbol{r}_\parallel} \psi_\nu(z)$ of $\mathcal{H}_{\text{qw}}$ (31). $\mathcal{E}_\nu$ (ψ_ν) is the νth confined energy level (wave function) of the well and $\sigma = \uparrow, \downarrow$ is the electron spin component along the z direction. Note that here we neglect the z dependence of the longitudinal and transverse effective masses. We then project the total 3D Hamiltonian (30) onto the basis set $\{|\boldsymbol{k}_\parallel \nu \sigma\rangle\}$.

Explicitly, the effective model with two subbands $\{|\boldsymbol{k}_\parallel 1\uparrow\rangle, |\boldsymbol{k}_\parallel 1\downarrow\rangle, |\boldsymbol{k}_\parallel 2\uparrow\rangle, |\boldsymbol{k}_\parallel 2\downarrow\rangle\}$, in the coordinate system $x||(100)$, $y||(010)$, can be written as

$$\mathcal{H}^{2\text{D}} = \begin{pmatrix} \mathcal{E}_{\boldsymbol{k}_\parallel 1} & i(\alpha_1 + \beta_1)k_- & 0 & i(\eta + \Gamma)k_- \\ -i(\alpha_1 + \beta_1)k_+ & \mathcal{E}_{\boldsymbol{k}_\parallel 1} & -i(\eta + \Gamma)k_+ & 0 \\ 0 & i(\eta + \Gamma)k_- & \mathcal{E}_{\boldsymbol{k}_\parallel 2} & i(\alpha_2 + \beta_2)k_- \\ -i(\eta + \Gamma)k_+ & 0 & -i(\alpha_2 + \beta_2)k_+ & \mathcal{E}_{\boldsymbol{k}_\parallel 2} \end{pmatrix}. \tag{49}$$

The two 2×2 blocks [upper left (α_1, β_1) and lower right (α_2, β_2)] of Eq. (49) correspond to the usual Rashba-Dresselhaus Hamiltonian coupled by the "off-diagonal" intersubband block (η, Γ). Note, however, that differently from zincblende case (see Refs. [20] and [14]), the Rashba and Dresselhaus terms have the same functional form.

The intrasubband (intersubband) Rashba α_ν (η) and Dresselhaus β_ν (Γ) SO couplings in Eq. (49) can be conveniently expressed in terms of the quantities

$$\eta_{\nu\nu'} = \langle \psi_\nu | \eta_{\text{BIA}}(z) + \eta_H \partial_z V_H(z) + \eta_w \partial_z V_{w-e}(z) | \psi_{\nu'} \rangle \tag{50}$$

and

$$\Gamma_{\nu\nu'} = \gamma \left(b \langle \psi_\nu | k_z^2 | \psi_{\nu'} \rangle - k_\parallel^2 \delta_{\nu\nu'} \right). \tag{51}$$

The Rashba couplings are $\alpha_\nu \equiv \eta_{\nu\nu}$, within each subband, and $\eta \equiv \eta_{12}$, between subbands. Similarly, the Dresselhaus intraband couplings are $\beta_\nu \equiv \Gamma_{\nu\nu}$ and the intersubband Dresselhaus coupling is $\Gamma \equiv \Gamma_{12}$. To calculate β_ν, we assume parabolic bands (in the absence of SO) and replace $k_\parallel$ in Eq. (51) by the Fermi wave vector $k_{F,\nu} = \sqrt{2\pi n_\nu}$, with n_ν the occupation of the νth subband. We obtain

$$\beta_\nu = \gamma \left(b \langle \psi_\nu | k_z^2 | \psi_\nu \rangle - 2\pi n_\nu \right). \tag{52}$$

This is a very good approximation as the Fermi contours are almost circles because the SO interaction strength is small as compared to the Fermi energy of the system. Similarly to zincblende structures the renormalized Dresselhaus coupling can, in principle, be tuned by a gate electrode controlling the electron density n_ν [9]. Note, however, that in contrast to zincblende structures, the entire in-plane part of the Dresselhaus term $[-\gamma k_\parallel^2$, Eq. (51)] in wurtzite quantum wells contributes to renormalize the usual "bare" linearized Dresselhaus term $\gamma b \langle \psi_\nu | k_z^2 | \psi_\nu \rangle$. As we will see below, this is a very important point as one can, in principle, tune the Rashba and Dresselhaus couplings to equal and opposite strengths—by changing the electron density [Eq. (52)] in single subband well systems for simplicity—and hence completely suppress spin-orbit interaction in wurtzite systems. In zincblende wells there is always a nonzero cubic anisotropic Dresselhaus term that becomes detrimental at high enough densities [9].

The Rashba coupling α_ν (η) can be written in terms of several contributions, i.e.,

$$\alpha_\nu = \alpha_\nu^{\text{BIA}} + \alpha_\nu^{\text{H}} + \alpha_\nu^{\text{w}}, \tag{53}$$

with

$$\alpha_\nu^{\text{BIA}} = \langle \psi_\nu | \eta_{\text{BIA}}(z) | \psi_\nu \rangle, \tag{54}$$

$$\alpha_\nu^{\text{H}} = \eta_H \langle \psi_\nu | \partial_z V_H(z) | \psi_\nu \rangle, \tag{55}$$

$$\alpha_\nu^{\text{w}} = \eta_w \langle \psi_\nu | \partial_z V_{w-e}(z) | \psi_\nu \rangle, \tag{56}$$

the bulk coefficient [49], the Hartree term, and the contribution due to the structural potential, respectively. The Hartree coefficient can also be split into different contributions [see Eq. (20)],

$$\alpha_\nu^{\text{H}} = \alpha_\nu^{\text{elect}} + \alpha_\nu^{\text{d}} + \alpha_\nu^{\text{int}} + \alpha_\nu^{\text{g}}, \tag{57}$$

where

$$\alpha_\nu^{\text{elect}} = \eta_H \langle \psi_\nu | \partial_z V_{\text{elect}}(z) | \psi_\nu \rangle, \tag{58}$$

$$\alpha_\nu^{\text{d}} = \eta_H \langle \psi_\nu | \partial_z V_{\text{d}}(z) | \psi_\nu \rangle, \tag{59}$$

$$\alpha_\nu^{\text{int}} = \eta_H \langle \psi_\nu | \partial_z V_{\text{int}}(z) | \psi_\nu \rangle, \tag{60}$$

$$\alpha_\nu^{\text{g}} = \eta_H \langle \psi_\nu | \partial_z V_{\text{g}}(z) | \psi_\nu \rangle \tag{61}$$

are due to, respectively, the purely electron Hartree potential, the doping potential, the internal potential (built-in electric fields), and the external gate potential. Note that all these SO coupling coefficients depend on the self-consistent potential and the subband wave functions.

Interestingly, as mentioned above, the Rashba and Dresselhaus terms induce the same electron spin configuration in a *c* axis oriented wurtzite structure [79–82], in contrast to the (001)-grown zincblende heterostructures. This allows us to define an effective SO coupling parameter for each subband

$$\alpha_\nu^{\text{eff}} = \alpha_\nu + \beta_\nu, \tag{62}$$

and similarly an effective intersubband SO coupling

$$\eta^{\text{eff}} = \eta + \Gamma. \tag{63}$$

Experimental measurements of the SO splittings [Shubnikov–de Haas oscillations or weak (anti) localization experiments] would probe, e.g., the effective coupling coefficient α_ν^{eff}. More importantly, one can possibly tune α_ν^{eff} to zero by varying the electron density, i.e.,

$$\alpha_\nu^{\text{eff}} = \alpha_\nu + \gamma \left(b \langle \psi_\nu | k_z^2 | \psi_\nu \rangle - 2\pi n_\nu \right) = 0. \tag{64}$$

For a single subband system ($\nu = 1$) and similarly to Refs. [80,81], we find that at the areal electron density

$$n_1 = \frac{\alpha_1}{2\pi\gamma} + \frac{b}{2\pi} \langle \psi_1 | k_z^2 | \psi_1 \rangle, \tag{65}$$

the SO term vanishes altogether up to cubic order, thus enhancing spin lifetimes in these systems [80,81]. Note that Eq. (65) has to be solved self-consistently as both sides depend on the density (i.e., the wave function ψ_1 also depends on the density n_1). It should be interesting to look for wurtzite materials in which Eq. (65) is obeyed.

In the following we evaluate all the relevant SO couplings defined above by self-consistently solving Schrödinger and Poisson coupled equations.

V. RESULTS AND DISCUSSIONS

Here we first introduce the structure of the quantum wells studied. Then we discuss our calculated SO couplings based on the model presented in the previous sections. Our discussions cover both the single and double well cases with either one or two occupied subbands.

A. Heterostructures

We consider GaN/Al$_x$Ga$_{1-x}$N heterostructures grown along the $z||[0001]$ direction. For the single well, our heterostructure is defined by a well of width $L_w = 10$ nm and two symmetric barrier regions of width $L_b = 7$ nm [see Fig. 1(b)]. Unless otherwise stated, the electron density is *fixed* at $n_e =$

TABLE II. Band parameters (in eV) for GaN/Al$_x$Ga$_{1-x}$N heterostructures, see the single well shown in Fig. 1(b).

x	$\delta_e(\delta_{be})$	$\delta_9(\delta_{bA})$	$\delta_B(\delta_{bB})$	$\delta_C(\delta_{bC})$
0.30	0.5252	0.2950	0.1546	0.2784
0.40	0.7051	0.4044	0.2098	0.3877
0.50	0.8876	0.5157	0.2059	0.4990
0.60	1.0728	0.6288	0.3228	0.6120
0.70	1.2608	0.7438	0.3805	0.7270
0.80	1.4515	0.8606	0.4391	0.8438

1.0×10^{12} cm^{-2}, arising from two symmetrically doped layers sitting 6 nm away from the center of the well. Our double well has a similar geometry, except for an additional barrier of width $L_{cb} = 2$ nm embedded in the center of the structure.

Wurtzite GaN-based heterostructures are usually grown on a GaN substrate by molecular beam epitaxy, i.e., the Al$_x$Ga$_{1-x}$N barriers are deformed and the corresponding lattice constant is adjusted to the GaN substrate and quantum wells [72,83,84], which is the case we consider here. In the Al$_x$Ga$_{1-x}$N layers [66], we choose the SO and the crystal field splitting parameters $\Delta_{\text{so}} = 0.014$ eV, $\Delta_{\text{cr}} = 0.019 - 0.183x$ eV, respectively, the lattice constant $A_l = 3.189 - 0.077x$ Å, the deformation potentials $D_1 = -3.0$ eV, $D_2 = 3.6$ eV, $D_3 = 8.82 + 0.78x$ eV, $D_4 = -4.41 + 0.39x$ eV (valence band), $a_{c1} = -9.5 - 2.5x$ eV, $a_{c2} = -8.2 + 2.8x$ eV (conduction band) [67], and the elastic constants $C_{13} = 106 + 2x$ GPa, $C_{33} = 398 - 25x$ GPa [85]. The unstrained band gap is $E_g = 3.507 + 2.723x$ eV and the strained one is calculated by taking into account the strain-induced band edge shifts (see Sec. II B 2). The spontaneous polarization is given by $-0.029 - 0.051x$ C m^{-2} and the piezoelectric coefficients by $e_{13} = -0.35 - 0.15x$ C m^{-2}, $e_{33} = 1.27 + 0.25x$ C m^{-2} [66].

The fraction of the s-p_z mixing we consider here is of $\sim1\%$. This is the same value used for ZnO, which has a very similar band gap. We then obtain $\Delta_{\text{sz}} \sim 0.467$ meV [35,86]. The interband Kane parameters are taken as $E_1 = E_2 = 14.0$ eV [65,66,87,88], with $E_{1,2} = 2m_0 P_{1,2}^2 / \hbar^2$, and are assumed the same in the well and barriers. We choose a uniform dielectric constant $\epsilon_r = 10.0$ [89] and consider the temperature $T = 2$ K. The relevant band parameters for GaN/Al$_x$Ga$_{1-x}$N heterostructures are shown in Table II for typical Al contents on the barriers [see Fig. 1(b)].

By inserting the relevant parameters listed above into Eqs. (32) and (33), we determine the out-of-plane $m_\perp(\text{GaN}) = 0.2014 m_0$ and in-plane $m_\parallel(\text{GaN}) = 0.2005 m_0$ effective masses, in excellent agreement with the experimental values $0.2m_0$ and $0.2m_0$ [66,90], respectively. We also calculate the Rashba SO parameters $\eta_{\text{BIA}}(\text{GaN}) = 1.938$ meV Å, $\eta_H = 0.01138$ meV Å^2, and $\eta_w = 2.462$ meV Å^2, see Eqs. (38)–(43). For the Dresselhaus parameters γ and b [see Eq. (44)], we use $\gamma = 0.32$ eV Å^3 and $b = 3.855$ [23,24].

B. Single well

Next we show our calculated SO coupling coefficients for a GaN/Al$_{0.3}$Ga$_{0.6}$N single well with one occupied subband. The dependence of these SO couplings on the Al content x on the Al$_x$Ga$_{1-x}$N layers is discussed as well.
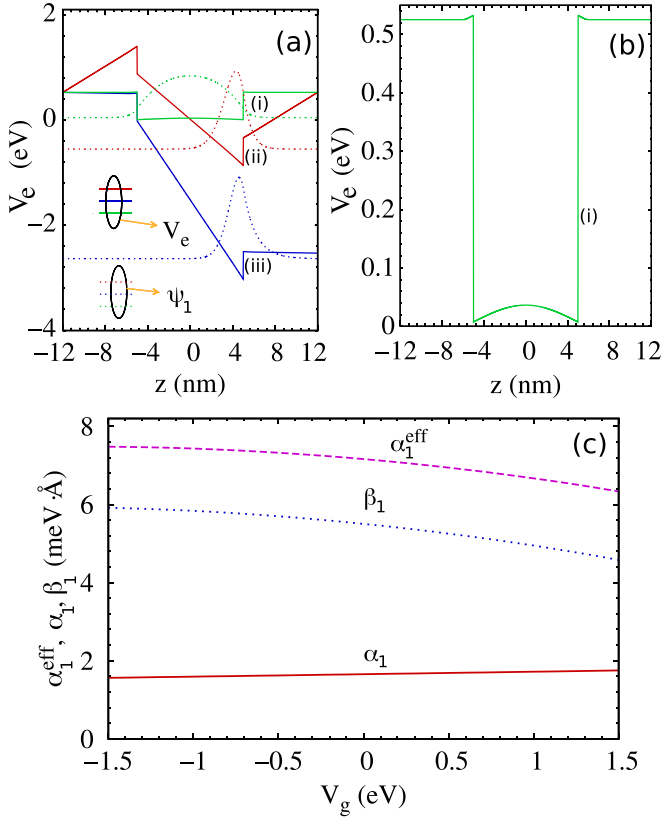
FIG. 2. (a) Self-consistent potential V_e (solid curves) and wave function profile ψ_1 of the first subband (dotted curves) for three different conditions of the built-in fields, for a GaN/Al$_{0.3}$Ga$_{0.7}$N single well at $V_g = 0$. (i) Green curves: zero built-in field (flat-band model); (ii) red curves: built-in field with periodic boundary conditions; and (iii) blue curves: built-in field with neutral surface charge boundary conditions. The energy levels (not shown) of the first subband for these three conditions are $\mathcal{E}_1 = 44.9, -551.2, -2634.2$ meV, respectively. (b) Blowup of the potential V_e in the flat-band model. (c) Rashba α_1, Dresselhaus β_1, and effective SO $\alpha_1^{\text{eff}} = \alpha_1 + \beta_1$ couplings as functions of V_g. The areal electron density is kept fixed at 1.0×10^{12} cm^{-2}, so that only the first subband is occupied. The temperature is $T = 2$ K.

We also determine the SO couplings of a GaN/Al$_{0.3}$Ga$_{0.6}$N well with two occupied subbands.

1. One occupied subband

Before discussing the SO couplings in detail, let us first have a look at our self-consistent solutions. Figure 2(a) shows the profiles of the conduction band potential V_e and of the first subband wave function of a GaN/Al$_{0.3}$Ga$_{0.7}$N single well with only one occupied subband. We consider three cases: (i) the flat-band model (no built-in field) (green curves), (ii) periodic boundary conditions (red curves), and (iii) neutral surface charge boundary conditions (blue curves).

We observe that the flat-band model produces the usual profile of a confining square well potential [see Fig. 2(b)] and its corresponding envelope wave function. In contrast, in the presence of the strong built-in field (spontaneous and piezoelectric, $\sim$MV/cm [70,87]), both the periodic and the neutral surface charge boundary conditions transform the
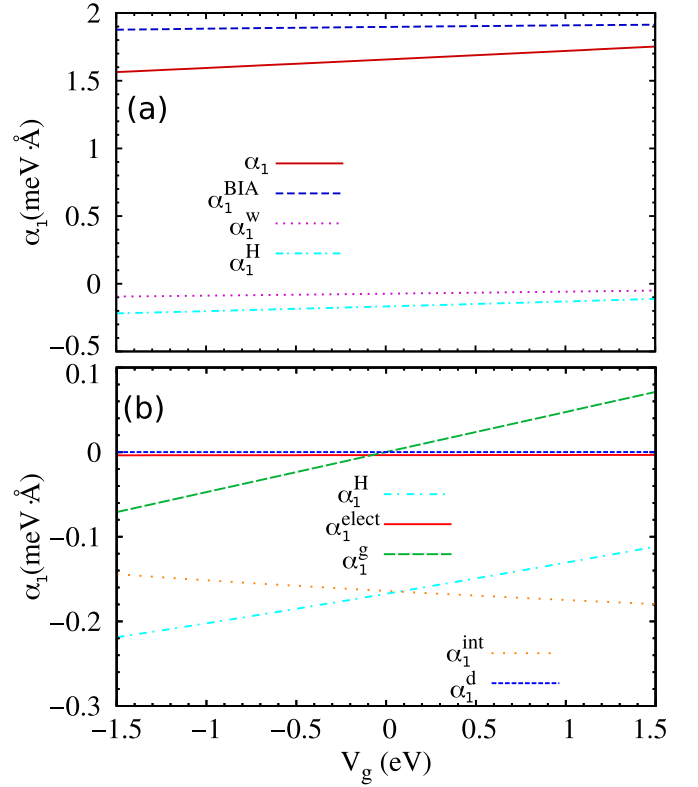
FIG. 3. (a) Rashba α_1 and its several contributions: the bulk α_1^{BIA}, the structural α_1^{w}, and the Hartree α_1^{H} contributions as functions of V_g in a GaN/Al$_{0.3}$Ga$_{0.7}$N single well with one occupied subband. (b) Contributions to α_1^{H}: the pure electron Hartree α_1^{elect}, the internal field α_1^{int}, the doping α_1^{d}, and the external gate α_1^{g} coefficients as functions of V_g. The areal electron density is held fixed at 1.0×10^{12} cm^{-2}. The temperature is $T = 2$ K.

rectangular-type well into a triangularlike one. Accordingly, electrons are mainly confined near one of the well/barrier interfaces. We find that the SO couplings calculated in GaN wells in both cases are comparable, the discrepancy being of just $\sim$0.2 meV Å. Thus in the following, we focus on the widely adopted periodic boundary conditions [91,92].

Figure 2(c) shows the Rashba α_1, Dresselhaus β_1, and effective SO $\alpha_1^{\text{eff}} = \alpha_1 + \beta_1$ couplings as functions of the gate voltage V_g. One can see that the Rashba term is relatively weaker than the Dresselhaus coupling, but their magnitudes are comparable. At zero bias $V_g = 0$, we obtain the total SO coupling intensity $\alpha_1^{\text{eff}} = 7.16$ meV Å, in agreement with results from weak antilocalization measurements, in which the spin splitting parameter was reported ranging from 5.5 to 10.01 meV Å [26–28,30,37]. In addition, we find that the Rashba coupling, which in general strongly depends on V_g in usual zincblende quantum wells, remains essentially constant as V_g varies. The weak dependence of α_1 on V_g follows from the interplay of its several different contributions, as we discuss next.

In Fig. 3(a) we show each contribution of α_1 as a function of V_g. Figure 3(b) further shows the several terms of α_1^{H} [see Eqs. (58)–(61)]. For the GaN and Al$_{0.3}$Ga$_{0.7}$N layers, we obtain $\alpha_1^{\text{BIA}}(\text{GaN}) = 1.938$ meV Å and $\alpha_1^{\text{BIA}}(\text{AlGaN}) = 1.570$ meV Å, respectively. Since the
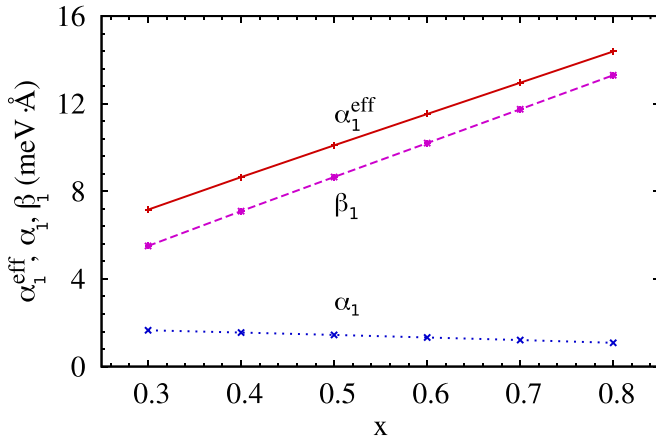
FIG. 4. Rashba α_1, Dresselhaus β_1, and the effective SO $\alpha_1^{\mathrm{eff}} = \alpha_1 + \beta_1$ strengths in GaN/Al$_x$Ga$_{1-x}$N single wells with one occupied subband as functions of the Al content x at $V_{\mathrm{g}} = 0$. The areal electron density n_e is held fixed at 1.0×10^{12} cm^{-2}. The temperature is $T = 2$ K.

wave function is mostly confined in the well (GaN layer), the intrinsic bulk contribution $\alpha_1^{\mathrm{BIA}}(\mathrm{GaN}) \approx \alpha_{\mathrm{bulk}}^{\mathrm{BIA}}$ remains essentially constant as V_{g} varies.

The combined contributions of the Hartree α_1^{H} and structural α_1^{w} terms refer to the usual Rashba coupling induced by the structural inversion asymmetry of the system. As can be seen in Figs. 3(a) and 3(b), the usual Rashba term is approximately one tenth of the bulk Rashba contribution. Therefore, the total Rashba coupling has a similar behavior with V_{g} as the bulk Rashba term, i.e., it is weakly gate dependent. In available reports on the SO coupling in wurtzite heterostructures concerning $\boldsymbol{k} \cdot \boldsymbol{p}$ interactions, however, the bulk Rashba term was missed [36,40,47]. On the other hand, we must emphasize that, even though the usual Rashba term is much weaker than the bulk Rashba coupling in GaN-based wurtzite wells, its contribution in relatively narrow gap semiconductors (e.g., GaAs in the wurtzite phase) can become important, thus possibly leading to a sensitive electrical control of it.

Let us now consider the effects on the SO couplings of the Al content on the Al$_x$Ga$_{1-x}$N layers. The Al x content modifies the strength of the built-in field and the band offsets of the well, consequently changing the SO couplings. Figure 4 shows α_1, β_1, and α_1^{eff} as functions of x at $V_{\mathrm{g}} = 0$. We find that the Dresselhaus coupling β_1 increases almost linearly with x. This is due to an increase of the piezoelectric polarization in the barriers as x varies, which makes the electrons more confined in the well. On the other hand, we observe that the Rashba term α_1 is not sensitive to x, again because of the dominant bulk contribution.

2. Two occupied subbands

Here we change the doping conditions so we can effectively occupy the second subband. In contrast to the case of one occupied subband, in which we have two symmetrically doped layers, we have now only a one-side doping layer (asymmetric doping), so that the doping field can partially compensate the built-in field, thus making the well confinement profile less steep. In addition, we increase the
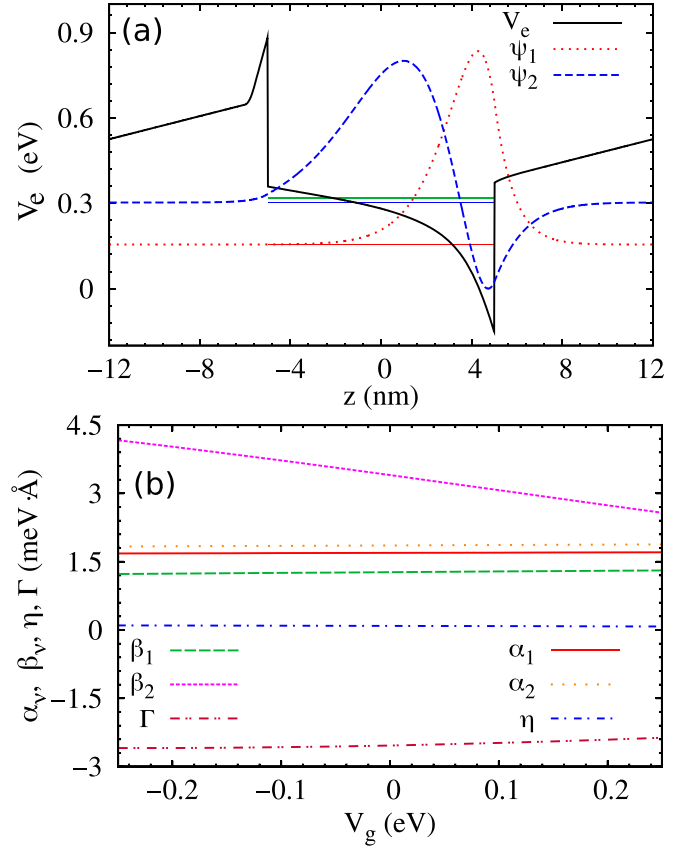

FIG. 5. (a) Self-consistent potential profile V_e and wave function profile of the first ψ_1 and second ψ_2 occupied subbands of a GaN/Al$_{0.3}$Ga$_{0.7}$N one-side doped single well at $V_{\mathrm{g}} = 0$. The horizontal blue, red, and green lines inside the well indicate the subband energy levels $\mathcal{E}_1 = 155.1$ meV, $\mathcal{E}_2 = 302.8$ meV, and the Fermi level $\mathcal{E}_{\mathrm{F}} = 318.5$ meV, respectively. (b) Intrasubband (intersubband) Rashba α_ν (η) and Dresselhaus β_ν (Γ) SO couplings as functions of V_{g}. The areal electron density is held fixed at $n_e = 1.5 \times 10^{13}$ cm^{-2}. The temperature is $T = 2$ K.

areal electron density to $n_e = 1.5 \times 10^{13}$ cm^{-2}. This corresponds to a higher doping density n_d in the doping layer. Since we assume $n_d = n_e$, we ensure charge neutrality in our system.

Figure 5(a) shows the self-consistent confining potential V_e and the wave function profile of the first ψ_1 and second ψ_2 occupied subbands of the well at $V_{\mathrm{g}} = 0$. Because of the change in the doping conditions, we observe that the well becomes flatter [cf. Figs. 2(a) and 5(a)]. In Fig. 5(b) we show the intrasubband Rashba α_ν and Dresselhaus β_ν, as well as the intersubband Rashba η and Dresselhaus Γ SO couplings as functions of V_{g}. The coupling α_ν depends very weakly on V_{g}, similarly to the case of one occupied subband [cf. Figs. 2 and 5], because of the dominant contribution of the bulk Rashba term. The various constituents of α_ν are not shown since they all have the same behavior as in the one occupied subband case.

As for the coupling β_ν, as the confining potential becomes flatter, we find that the first subband term β_1 is around four times weaker than that in the well with only one subband occupied. In addition, β_1 remains almost constant as V_{g} varies.

On the other hand, for the second subband, β_2 is relatively sensitive to V_g. We attribute the different behaviors of β_1 and β_2 with V_g, to the distinct distributions of electrons occupying the first and second subbands. Electrons occupying the first subband are mostly confined to the right well/barrier interface (i.e., a narrow triangular confinement) [see ψ_1 in Fig. 5(a)], and cannot "feel" an overall modification of the potential due to V_g. However, electrons occupying the second band spread almost all over the whole well region [see ψ_2 in Fig. 5(a)]. Thus, the second subband wave function profile ψ_2 is more strongly dependent on V_g, further leading $\beta_2 = \gamma(b\langle\psi_2|k_z^2|\psi_2\rangle - k_{F,2}^2)$ to be more sensitive to V_g as compared to β_1 [see Fig. 5(b)]. Here $k_{F,\nu} = \sqrt{2\pi n_\nu}$ is the Fermi wave vector of the νth subband and n_ν its occupation.

The intersubband Rashba coupling strength η is much weaker than the intrasubband coupling α_ν. We attribute this to the fact that the bulk intersubband Rashba contribution $\eta^{\text{BIA}} = \langle\psi_1|\eta_{\text{BIA}}(z)|\psi_2\rangle$ to η is negligible, as electrons are mostly confined inside the well. More specifically, we have $\eta^{\text{BIA}} = \langle\psi_1|\eta_{\text{BIA}}(z)|\psi_2\rangle \approx \langle\psi_1|\eta_{\text{BIA}}(\text{well})|\psi_2\rangle \sim 0$ [see Eq. (39)]. Note that for α_ν, the bulk term α_{nu}^{BIA} dominates over the usual Rashba contributions. On the other hand, for the intersubband Dresselhaus term $\Gamma = \langle\psi_1|k_z^2|\psi_2\rangle$, we find that it is comparable to β_ν. We should emphasize that Γ vanishes in the symmetric configuration because of parity. Here Γ is nonzero at $V_g = 0$, due to the presence of both the built-in field and the asymmetric one-side doping field.

C. Double well

In this section we focus on obtaining the SO couplings for the double quantum well GaN/Al$_{0.3}$Ga$_{0.7}$N with an Al$_x$Ga$_{1-x}$N central barrier (see Sec. V A).

Before discussing the SO couplings in detail, let us first have a look at how the Al content in the central barrier affects the double well configuration. At low Al concentration, we find that the electrons are mostly confined to one side [right side of our wells, see Fig. 6(a)] of the system, due to the presence of the strong built-in field, which makes the double well essentially an *effective* single well. Figure 6(a) shows the electron confining potential V_e and the wave function profiles ψ_ν ($\nu = 1, 2$) of the lowest two subbands in a double well with $x = 0.3$ in the central barrier. Although only one subband is occupied in this configuration, for comparison, we also show ψ_2 for the empty second level of the well. As can be easily seen, this double well configuration is essentially similar to the ones of the single wells discussed in previous sections.

If we further increase the Al content in the central barrier, we find that the left and right sides of the double well compete to confine the electrons. Interestingly, when $x \sim 0.69$, a *seemingly* symmetric configuration occurs. In Fig. 6(b) we show the corresponding confining potential and the wave function profiles at this configuration with two occupied subbands. We can see that the electrons occupying the two subbands are almost equally distributed on the left and right sides of the well, in contrast to the case of smaller values of x [cf. Figs. 6(a) and 6(b)]. However, we emphasize that this seemingly symmetric configuration (at $x = 0.69$) is actually structurally asymmetric, since the gradient of the potential
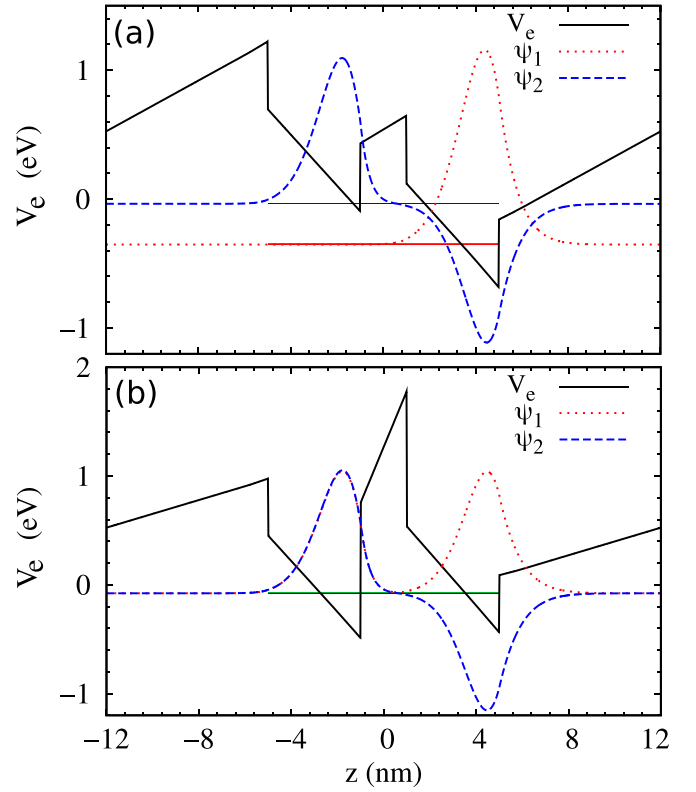

FIG. 6. Self-consistent potential V_e and wave function profiles ψ_ν ($\nu = 1, 2$) of a GaN/Al$_{0.3}$Ga$_{0.7}$N double well with an Al$_x$Ga$_{1-x}$N central barrier at $V_g = 0$. (a) One occupied subband with $x = 0.3$ in the central barrier; (b) two occupied subbands with $x = 0.69$ in the central barrier. For comparison, in (a) it is shown the second subband wave function ψ_2 for the empty second level. The horizontal blue, red, and green lines inside the well indicate the subband energy levels $\mathcal{E}_1$, $\mathcal{E}_2$, and the Fermi level $\mathcal{E}_F$, respectively. In (a), $\mathcal{E}_1 = -352.3$ meV, $\mathcal{E}_2 = -336.6$ meV, and $\mathcal{E}_F = -340.4$ meV; in (b), $\mathcal{E}_1 = -78.2$ meV, $\mathcal{E}_2 = -78.2$ meV, and $\mathcal{E}_F = -72.2$ meV. The areal electron density n_e is held fixed at 1.0×10^{12} cm^{-2}.

(i.e., the electric field) has the same sign (negative) on the left and right wells, see Fig. 6(b). Next we determine the SO coupling coefficients for this configuration and discuss how these change with V_g.

Figure 7(a) shows $\alpha_\nu = \alpha_\nu^{\text{BIA}} + \alpha_\nu^{\text{H}} + \alpha_\nu^{\text{w+b}}$ and their several different contributions: α_ν^{BIA}, α_ν^{H}, and $\alpha_\nu^{\text{w+b}}$, with $\alpha_\nu^{\text{w+b}} \equiv \alpha_\nu^{\text{w}} + \alpha_\nu^{\text{b}}$, for each subband $\nu = 1, 2$. Note that the structural term in a double well has an additional contribution $\alpha_\nu^{\text{b}} = \eta_{\text{b}}\langle\nu|\frac{dV_b(z)}{dz}|\nu\rangle$ due to the presence of the central barrier [19]. The potential $V_b(z)$ describes the structural potential between the well and the central barrier. Straightforwardly, η_b has the same expression as η_w [see Eq. (37)] with the well offsets δ_i being replaced by the central barrier offsets δ_{bi}. Similarly to the case of single wells, we find that α_ν remains essentially constant as a function of V_g, since the bulk contribution (not sensitive to V_g) dominates over all the other contributions. Interestingly, we find that α_1 and α_2 almost interchange their respective values, across the seemingly symmetric configuration (at $V_g = 0$), because electrons occupying the first and second subbands interchange their distributions for $V_g > 0$ and $V_g < 0$. This feature of interchanging values across $V_g = 0$
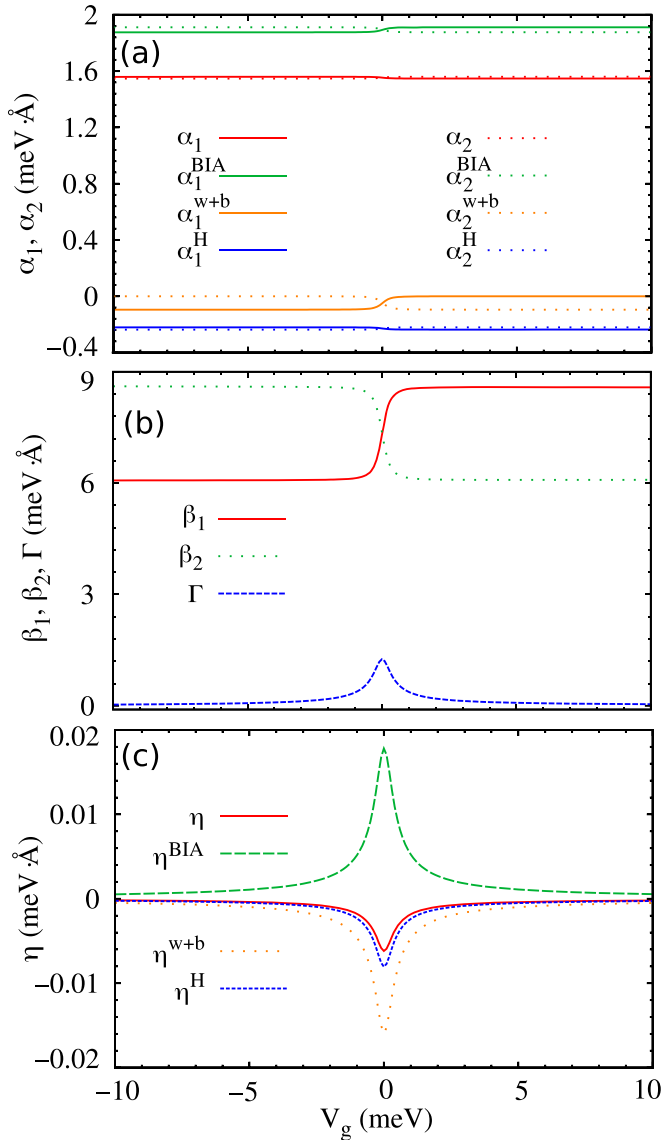
FIG. 7. (a) Intrasubband Rashba couplings α_ν ($\nu = 1, 2$) for a GaN/Al$_{0.3}$Ga$_{0.7}$N double well with an Al$_{0.69}$Ga$_{0.31}$N central barrier as functions of V_g. Several distinct constituents of α_ν: the bulk α_ν^c, the structural α_ν^w, and the total Hartree α_ν^H contributions. (b) Intrasubband β_ν and intersubband Γ Dresselhaus SO strengths as functions of V_g. (c) Intersubband η and its various contributions versus V_g. The areal electron density is held fixed at 1.0×10^{12} cm^{-2}.

also holds for the Dresselhaus terms β_1 and β_2, with even more pronounced behavior (cf. α_ν's), as shown in Fig. 7(b).

In Figs. 7(b) and 7(c) we show the intersubband Dresselhaus Γ and the Rashba η couplings, respectively, as functions of V_g. We find that both η and Γ achieve their maximal strength at $V_g = 0$, in contrast to the intrasubband α_ν and β_ν. This arises from the intersubband SO couplings depending on the overlap of the wave functions ψ_1 and ψ_2 of the two subbands, see Eqs. (50) and (51). At $V_g = 0$ (seemingly symmetric configuration), ψ_1 and ψ_2 have a perfect overlap. However, away from $V_g = 0$, ψ_1 and ψ_2 are largely separated, i.e., one is mostly confined in the left well and the other in the right well.

On the other hand, for large Al concentration in the central barrier ($x \sim 0.84$), we find that the one subband electron occupation is restored (for the same areal electron density), similarly to the case of low x mentioned previously, except that we have an almost reversed configuration of the left and right wells constituting the double well structure.

VI. CONCLUDING REMARKS

We have derived a very general SO Hamiltonian for conduction electrons in wurtzite heterostructures valid for arbitrary confining potentials (quantum wells, wires, and dots) and external magnetic fields. Our starting point is the 8×8 Kane model including the s-p_z orbital mixing relevant to wurtzite systems. We then obtain a 2×2 effective SO Hamiltonian by applying both the Löwdin perturbation theory and the folding down approach. For concreteness, we focus on GaN/AlGaN wells and investigate in detail the electron SO couplings.

In addition to the s-p_z orbital mixing (absent in zincblende structures), we have taken into account the renormalization of the conduction band spinor component when deriving the effective 2×2 electron Hamiltonian for heterostructures; these two elements were not included in previous works. Most importantly, we find that these are crucial ingredients in obtaining the BIA Rashba and BIA Dresselhaus terms in quantum wells, and in deriving an effective electron Hamiltonian energy independent (i.e., an *effective* Schrödinger-type equation).

Through a self-consistent Schrödinger-Poisson calculation on GaN/AlGaN both single and double wells, involving either one or two occupied subbands, we have determined all the relevant SO strengths, i.e., the intrasubband Rashba α_ν ($\nu = 1, 2$) and Dresselhaus β_ν couplings, as well as the intersubband Rashba η and Dresselhaus Γ couplings. We have also determined the several distinct constituents of the SO couplings due to the bulk, the Hartree, and the structural contributions, and find that the SO couplings follow from the interplay of all these terms. Particularly, we find that the bulk Rashba term α_ν^{BIA} dominates over all other remaining contributions to the intrasubband Rashba couplings. Our calculated spin-orbit coupling is in agreement with experimental data for single wells. For our double wells, we find a *seemingly* symmetric configuration, at which both the intersubband Rashba and Dresselhaus couplings assume their largest values, due to a perfect overlap of the wave functions of the two subbands. On the other hand, across this configuration when we vary V_g, the intrasubband Dresselhaus couplings β_1 and β_2 almost interchange their values, a similar behavior also occurring for the Rashba couplings α_1 and α_2. In addition, we have derived an effective spin-orbit Hamiltonian for electrons with arbitrary confining potentials and external magnetic fields, valid for quantum wells, wires, and dots.

As a final remark, although the SO couplings in our GaN wells are not sensitive (except for the double well around the seemingly symmetric configuration) to V_g, we emphasize that a sensitive electrical control of the Rashba couplings could be possible in narrow-gap wurtzite wells (e.g., GaAs with wurtzite structure), where the usual Rashba contributions (sensitive to V_g) could be comparable or even larger than the bulk contribution. Accordingly, since the

Rashba and Dresselhaus SO fields have the same functional form, it should be easy to attain both the weak and strong SO regimes, via a sensitive electrical control of the Rashba couplings (both magnitude and sign). More interesting, it may be possible to tune $\alpha = -\beta$ in some parameter range, which would lead to a complete cancellation of the Rashba and Dresselhaus terms [see Eq. (65)], thus rendering the spin a conserved quantity in wurtzite wells. This could possibly extend the SO-induced spin-flip times [80,81] as compared to zincblende structures. Additional work is needed to investigate this exciting possibility.

We hope that our general effective SO Hamiltonian stimulate further theoretical studies involving quantum wires and dots in wurtzite systems; these may be relevant, for instance, to wurtzite dot qubits and Majorana nanowires.

APPENDIX A: EFFECTIVE MODELS VIA GROUP THEORY AND $\boldsymbol{k} \cdot \boldsymbol{p}$

As discussed in the main text, there are many different approaches in the literature to describe the band structure of a wurtzite crystal. Indeed, its bulk Hamiltonian has been written in many different basis sets [54], which might lead to inconsistencies among the models. In the main text, we have shown a comprehensive and detailed derivation of effective models for bulk wurtzite, as well as heterostructures (quantum wells, wires, and dots). In this Appendix we complement our discussion with a full and systematic derivation of the 2×2 electronic model and the 8×8 Kane Hamiltonian using group theory methods combined with the $\boldsymbol{k} \cdot \boldsymbol{p}$ approach. This provides a deeper understanding of the s-p_z mixing and justifies the choice of basis shown in Table I.

First, we present an alternative derivation of the effective electron Hamiltonian $\mathcal{H}(k_x, k_y)$ for the conduction band of wurtzite quantum wells near the Γ point. Next, we derive the 8×8 Kane model for bulk wurtzite. More specifically, we start with the CC basis [40], listed in the second column of Table III, and then discuss the transformation to the primed basis CC′, third column of Table III, which is the basis set we use throughout the main text (Sec. II B). As we will see below, the S' and Z' orbitals arise from the s-p_z mixing discussed in Ref. [35]. It is important to track the effects of this hybridization to establish all matrix elements allowed by symmetry and identify systematically the approximations used to obtain the final Kane model for wurtzite crystals.

The last column in Table III shows the irreducible representations (IRREPs) of the orbital part of the basis functions. Notice that, while zincblende crystals belong to the cubic T_d group, the wurtzite lattice belongs to the C_{6v}^4. For T_d, the directions x, y, and z are all equivalent. However,

TABLE III. CC basis without $|\nu\rangle$ and with $|\nu'\rangle$ the s-p_z hybridization. Normalization requires $|q_s|^2 + |q_z|^2 = 1$. The q_s and q_z coefficients here match those of Ref. [35]. The orbitals S and Z belong to the IRREP Γ_1 (transform as scalars), while X and Y combine to form Γ_5 [transform as a (x, y) vector].

ν	$|\nu\rangle$	$|\nu'\rangle$	C_{6v} IRREP
1	$|iS\uparrow\rangle$	$|iS'\uparrow\rangle = q_s|iS\uparrow\rangle + iq_z|Z\uparrow\rangle$	Γ_1
2	$|iS\downarrow\rangle$	$|iS'\downarrow\rangle = q_s|iS\downarrow\rangle + iq_z|Z\downarrow\rangle$	Γ_1
3	$-\frac{1}{\sqrt{2}}|X+iY\uparrow\rangle$	$-\frac{1}{\sqrt{2}}|X+iY\uparrow\rangle$	Γ_5
4	$+\frac{1}{\sqrt{2}}|X-iY\downarrow\rangle$	$+\frac{1}{\sqrt{2}}|X-iY\downarrow\rangle$	Γ_5
5	$+\frac{1}{\sqrt{2}}|X-iY\uparrow\rangle$	$+\frac{1}{\sqrt{2}}|X-iY\uparrow\rangle$	Γ_5
6	$-\frac{1}{\sqrt{2}}|X+iY\downarrow\rangle$	$-\frac{1}{\sqrt{2}}|X+iY\downarrow\rangle$	Γ_5
7	$|Z\uparrow\rangle$	$|Z'\uparrow\rangle = q_s|Z\uparrow\rangle + iq_z|iS\uparrow\rangle$	Γ_1
8	$|Z\downarrow\rangle$	$|Z'\downarrow\rangle = q_s|Z\downarrow\rangle + iq_z|iS\downarrow\rangle$	Γ_1

on C_{6v} there is no symmetry constraint in the z direction, which makes the S and Z orbitals equivalent in terms of their symmetries (both belong to Γ_1). This reduced symmetry leads to the appearance of extra finite terms on wurtzite crystals. Nonetheless, this broken symmetry along the z axis can be considered "small" (quasicubic approximation [54]). Therefore, all new terms are expected to be small or negligible. Here, however, we present all these new terms allowed by symmetry and show their $\boldsymbol{k} \cdot \boldsymbol{p}$ expressions.

1. Theory of invariants

The theory of invariants [16,35,55] allows us to search for the most general form of the Hamiltonian $\mathcal{H}(\boldsymbol{k})$ allowed by the symmetries of the crystal. Namely, we can write

$$\mathcal{H}(\boldsymbol{k}) = \sum_{i,j,l} H_{i,j,l}\, k_x^i\, k_y^j\, k_z^l, \tag{A1}$$

where $H_{i,j,l}$ are arbitrary matrices to be found. For 2D systems one can simply drop k_z and the sum over l.

The group of the Schrödinger equation is composed by the set of symmetry operations $\{O_i\}$ that keeps the crystal invariant. Consequently, these operations must commute with the Hamiltonian operator, yielding

$$\mathcal{H}(\boldsymbol{k}) = D_\psi(O_i)\,\mathcal{H}\big(D_k^{-1}(O_i)\boldsymbol{k}\big)\,D_\psi^{-1}(O_i), \tag{A2}$$

in which $D_\psi(O_i)$ and $D_k(O_i)$ are the matrix representations of O_i in the Hilbert and k spaces, respectively. For each O_i, this imposes constraints on $\mathcal{H}(\boldsymbol{k})$, which can be then written as a system of coupled equations solved to find the allowed terms in each $H_{i,j,l}$.

The matrix representations of $D_\psi(O_i)$ and $D_k(O_i)$ can be found on the Bilbao Crystallographic Server [93–95]. These can be applied to the QSYMM [96] python package that solves the constraints imposed by Eq. (A2) and returns the most general expressions allowed by symmetry for $H_{i,j,l}$.

2. 2×2 electronic effective model

Let us now apply the theory of invariants to find the effective 2×2 model for the conduction bands of our 2DEG

$\mathcal{H}(k_x, k_y)$ [for comparison, see upper left block of Eq. (49), i.e., the one-subband case] and of our 3D bulk Hamiltonian $\mathcal{H}(k_x, k_y, k_z)$ [cf., Eq. (21)]. The theory of invariants provides the general form allowed by symmetry for these models. In the main text, we complement this analysis by using the $\boldsymbol{k} \cdot \boldsymbol{p}$ approach to find expressions for the effective parameters in terms of the bulk matrix elements of the 8×8 Kane model.

a. Model for single-subband 2DEGs

Some materials, e.g., GaN and AlGaN, crystallize into the wurtzite structure, which belongs to the C_{6v}^4 (or $P6_3mc$) nonsymmorphic space group [55,57]. For quantum wells grown along the [0001] (*c* axis) crystallographic direction, this space group symmetry is maintained. At the Γ point, the first conduction subbands are spin degenerate. Their orbital components transform as scalars (trivial representation Γ_1), while the spinors transform as the $D_{1/2}$ double group IRREP, which is given by the generators of the SU(2). These are equivalent to the $D_{1/2}$ IRREP of the symmorphic group C_{6v}. For simplicity, we use the point group notation for the operations $\{O_i\} = \{E, 2C_6, 2C_3, C_2, 3\sigma_d, 3\sigma_v\}$. In practice, it is sufficient to consider the generators $\{C_6, \sigma_d\}$, which correspond, respectively, to the sixfold rotations around the z axis and the $x \to -x$ mirror operations. Additionally, we also consider time-reversal symmetry $\mathcal{T}$. In the Hilbert space, these read

$$D_\psi(C_6) = \pm \exp\left(i\frac{\pi}{6}\sigma_z\right), \tag{A3}$$

$$D_\psi(\sigma_d) = \pm \exp\left(i\frac{\pi}{2}\sigma_x\right), \tag{A4}$$

$$D_\psi(\mathcal{T}) = i\sigma_y\mathcal{K}, \tag{A5}$$

where $\mathcal{K}$ is the complex conjugate, and the $\pm$ signs refer to the 2π and 4π SU(2) rotations. On the other hand, for the k-space representation, with $\boldsymbol{k} = (k_x \quad k_y)^T$, we have

$$D_k(C_6) = \begin{bmatrix} \cos\left(\frac{2\pi}{6}\right) & \sin\left(\frac{2\pi}{6}\right) \\ -\sin\left(\frac{2\pi}{6}\right) & \cos\left(\frac{2\pi}{6}\right) \end{bmatrix}, \tag{A6}$$

$$D_k(\sigma_d) = -\sigma_z, \tag{A7}$$

$$D_k(\mathcal{T}) = -1_{2\times 2}. \tag{A8}$$

Substituting these representations into Eq. (A2), we find

$$H_{0,0} = h_0 1_{2\times 2}, \tag{A9}$$

$$H_{1,0} = h_1 \sigma_y, \tag{A10}$$

$$H_{0,1} = -h_1 \sigma_x, \tag{A11}$$

$$H_{1,1} = 0_{2\times 2}, \tag{A12}$$

$$H_{2,0} = H_{0,2} = h_2 1_{2\times 2}, \tag{A13}$$

$$H_{3,0} = h_3 \sigma_y \tag{A14}$$

$$H_{0,3} = -h_3 \sigma_x \tag{A15}$$

$$H_{2,1} = -h_3 \sigma_x \tag{A16}$$

$$H_{1,2} = h_3 \sigma_y \tag{A17}$$

with h_0, h_1, h_2, and h_3 arbitrary parameters. We can choose $h_0 = 0$, as it just results in an overall rigid shift. Moreover, we can identify $h_1 = \bar{\alpha}$, $h_2 = \hbar^2/2m^*$, and $h_3 = \bar{\beta}$, yielding

$$\mathcal{H}(k_x, k_y) = \frac{\hbar^2}{2m^*}\left(k_x^2 + k_y^2\right) + \bar{\alpha}(k_x\sigma_y - k_y\sigma_x)$$
$$+ \bar{\beta}\left(k_x^2 + k_y^2\right)(k_x\sigma_y - k_y\sigma_x). \tag{A18}$$

The effective mass m^* and the spin-orbit coupling $\bar{\alpha}$ and $\bar{\beta}$ here remain as unknown parameters. These can be obtained by fitting *ab initio* or experimental data. A more insightful approach, however, is to start from the 8×8 Kane model—derived in Sec. A 3—and project its solutions onto the electron subspace as developed in the main text.

b. Model for 3D bulk

As already mentioned above, the wurtzite bulk crystal belongs to the C_{6v}^4 space group. Considering that the conduction band transforms as $D_{1/2}$, it follows that the basis functions for the Hilbert space transform as the representations given for $D_\psi(C_6)$, $D_\psi(\sigma_d)$, and $D_\psi(\mathcal{T})$ in Eqs. (A3)–(A5), respectively. However, we are now dealing with a 3D space with $k = (k_x, k_y, k_z)$, and the k-space representations become

$$D_k(C_6) = \begin{bmatrix} \cos\left(\frac{2\pi}{6}\right) & \sin\left(\frac{2\pi}{6}\right) & 0 \\ -\sin\left(\frac{2\pi}{6}\right) & \cos\left(\frac{2\pi}{6}\right) & 0 \\ 0 & 0 & 1 \end{bmatrix}, \tag{A19}$$

$$D_k(\sigma_d) = \text{diag}[-1, 1, 1], \tag{A20}$$

$$D_k(\mathcal{T}) = -1_{3\times 3}. \tag{A21}$$

Using these representations in Eq. (A2), we obtain

$$\mathcal{H}(k_x, k_y, k_z) = \frac{\hbar^2}{2m_\parallel}k_\parallel^2 + \frac{\hbar^2}{2m_\perp}k_z^2 + (\sigma_x k_y - \sigma_y k_x)$$
$$\times \left[\alpha_{\text{bulk}}^{\text{BIA}} + \gamma\left(bk_z^2 - k_\parallel^2\right)\right], \tag{A22}$$

where the unknown coefficients $m_\perp$, $m_\parallel$, $\alpha_{\text{bulk}}^{\text{BIA}}$, γ, and b were chosen so that the notation is the same as that used in Eqs. (22), (25), and (26). As previously noted, the expressions for these coefficients were obtained in the main text through the $\boldsymbol{k} \cdot \boldsymbol{p}$ approach, see Eqs. (23), (24), (27)–(29).

3. 8 × 8 Kane model: Method of invariants

We apply the method of invariants to obtain the most general 8×8 Kane model considering the basis states shown in Table III. Differently from the previous section, here we follow a single group formulation, which matches the CC basis, and maintain the spins along z as good quantum numbers for the basis set. The representations for the generators $\{C_6, \sigma_d\}$ and the time-reversal operator $\mathcal{T}$ follow from the IRREPs Γ_1 and Γ_5 of the C_{6v} point group. Applying the constraints of the theory of invariants, we obtain the following 8×8 model in

the CC basis $|\nu\rangle$

$$
H_{8\times8} = \begin{pmatrix}
c_0 & 0 & 0 & 0 & 0 & ic_5 & ic_6 & 0 \\
0 & c_0 & 0 & 0 & ic_5 & 0 & 0 & ic_6 \\
0 & 0 & c_1 & 0 & 0 & 0 & 0 & 0 \\
0 & 0 & 0 & c_1 & 0 & 0 & 0 & 0 \\
0 & -ic_5 & 0 & 0 & c_2 & 0 & 0 & c_3 \\
-ic_5 & 0 & 0 & 0 & 0 & c_2 & c_3 & 0 \\
-ic_6 & 0 & 0 & 0 & 0 & c_3 & c_4 & 0 \\
0 & -ic_6 & 0 & 0 & c_3 & 0 & 0 & c_4
\end{pmatrix}
+
\begin{pmatrix}
0 & ic_7^- & c_{13}^+ & 0 & -c_{14}^- & 0 & 0 & -c_{15}^- \\
-ic_7^+ & 0 & 0 & -c_{13}^- & 0 & c_{14}^+ & c_{15}^+ & 0 \\
c_{13}^- & 0 & 0 & 0 & 0 & ic_8^- & ic_9^- & 0 \\
0 & -c_{13}^+ & 0 & 0 & -ic_8^- & 0 & 0 & ic_9^- \\
-c_{14}^+ & 0 & 0 & +ic_8^+ & 0 & -ic_{10}^- & -ic_{11}^- & 0 \\
0 & c_{14}^- & -ic_8^+ & 0 & +ic_{10}^+ & 0 & 0 & ic_{11}^- \\
0 & c_{15}^- & -ic_9^+ & 0 & +ic_{11}^+ & 0 & 0 & ic_{12}^- \\
-c_{15}^+ & 0 & 0 & -ic_9^+ & 0 & -ic_{11}^+ & -ic_{12}^+ & 0
\end{pmatrix} k_\pm
$$

$$
+
\begin{pmatrix}
0 & 0 & 0 & 0 & 0 & c_{16} & c_{17} & 0 \\
0 & 0 & 0 & 0 & c_{16} & 0 & 0 & c_{17} \\
0 & 0 & 0 & 0 & 0 & 0 & 0 & 0 \\
0 & 0 & 0 & 0 & 0 & 0 & 0 & 0 \\
0 & c_{16} & 0 & 0 & 0 & 0 & 0 & ic_{18} \\
c_{16} & 0 & 0 & 0 & 0 & 0 & ic_{18} & 0 \\
c_{17} & 0 & 0 & 0 & 0 & -ic_{18} & 0 & 0 \\
0 & c_{17} & 0 & 0 & -ic_{18} & 0 & 0 & 0
\end{pmatrix} k_z, \tag{A23}
$$

where c_n, $n = 0, \dots, 18$, are unknown coefficients allowed by symmetry, which later on will be defined in terms of the $\boldsymbol{k} \cdot \boldsymbol{p}$ parameters. The first matrix above corresponds to the k-independent terms, the second matrix gives the terms $c_n^\pm$ linear in $k_\pm = k_x \pm ik_y$, and the third matrix represents the k_z-linear terms. For simplicity, we do not show the k_x^2, k_y^2, and k_z^2 terms.

The model in Eq. (A23) is built solely based on the symmetries of the basis set. However, the IRREPs that define the $|\nu\rangle$ and $|\nu'\rangle$ basis sets are the same, as shown in Table III. Hence, up to this point, the model above does not distinguish between different basis sets with equivalent symmetries. To proceed we must specify the basis and identify the matrix elements c_n in terms of the $\boldsymbol{k} \cdot \boldsymbol{p}$ theory.

4. 8 × 8 Kane model: k · p approach

Here we consider $H = H_0^{\mathrm{CC}} + W^{\mathrm{CC}}(\boldsymbol{k})$, with

$$
H_0^{\mathrm{CC}} = \frac{p^2}{2m_0} + V(\boldsymbol{r}) + H_{\mathrm{soz}}, \tag{A24}
$$

$$
W^{\mathrm{CC}}(\boldsymbol{k}) = \frac{\hbar}{m_0} \boldsymbol{k} \cdot \boldsymbol{\pi} + H_{\mathrm{sox}} + H_{\mathrm{soy}}, \tag{A25}
$$

$$
H_{\mathrm{so}j} = C [\nabla V(\boldsymbol{r}) \times \boldsymbol{p}]_j \, \sigma_j, \tag{A26}
$$

$$
\boldsymbol{\pi} = \boldsymbol{p} + C[\boldsymbol{\sigma} \times \nabla V(\boldsymbol{r})], \tag{A27}
$$

where $C = \hbar/4m_0^2 c^2$ defines the SO coupling intensity.

Below we first show how a commutator trick [35] can be used to simplify some matrix elements and later we identify the matrix elements using the $\boldsymbol{k} \cdot \boldsymbol{p}$ model above.

a. Selection rules and commutator trick

As shown in Eq. (A24), we choose to keep only the z component of H_{so} in H_0^{CC}, such that the spin remains a good quantum number. In addition, this choice allows us to use a commutator trick introduced in Ref. [35] to eliminate a few

matrix elements. Namely, the matrix elements of $C\sigma_x V_z \equiv C\sigma_x \partial_z V$, which can be written as

$$
C\langle \nu_1 \uparrow | \sigma_x V_z | \nu_2 \downarrow \rangle = C\langle \nu_1 \uparrow | V_z | \nu_2 \uparrow \rangle \tag{A28}
$$

or

$$
\begin{aligned}
C\langle \nu_1 \uparrow | \sigma_x V_z | \nu_2 \downarrow \rangle &= -\frac{i}{\hbar} C\langle \nu_1 \uparrow | [V, p_z] | \nu_2 \uparrow \rangle \\
&= -\frac{i}{\hbar} C\langle \nu_1 \uparrow | [H_0^{\mathrm{CC}} - H_{\mathrm{soz}}, p_z] | \nu_2 \uparrow \rangle \\
&= -\frac{i}{\hbar} C\big[(\varepsilon_{\nu_1 \uparrow} - \varepsilon_{\nu_2 \uparrow}) \langle \nu_1 \uparrow | p_z | \nu_2 \uparrow \rangle \\
&\quad - \langle \nu_1 \uparrow | [H_{\mathrm{soz}}, p_z] | \nu_2 \uparrow \rangle \big] \\
&= \frac{i}{\hbar} C\langle \nu_1 \uparrow | [H_{\mathrm{soz}}, p_z] | \nu_2 \uparrow \rangle. \tag{A29}
\end{aligned}
$$

Here $|\nu\sigma\rangle$ are the eigenstates of H_0^{CC} with eigenenergies $\varepsilon_{\nu\sigma}$. Similar expressions hold for the matrix elements of $C\sigma_y V_z$. In Eq. (A28) we have simply acted σ_x on the ket, while in Eq. (A29), we have used the identity $\partial_z V \equiv -i[V, p_z]/\hbar \equiv -i[H_0^{\mathrm{CC}} - H_{\mathrm{soz}}, p_z]$. The last line in Eq. (A29) is only valid if the eigenstates are degenerate, i.e., $\varepsilon_{\nu_1 \uparrow} = \varepsilon_{\nu_2 \uparrow}$. Below we show that this type of matrix element, either in the form (A28) or (A29), is identically zero or negligible.

Let us first consider the matrix element in the form (A28). The operator V_z transforms as Γ_1, while the eigenstates transform either as Γ_1 or Γ_5 (see Table III). Therefore, the selection rules already dictate that the matrix element is zero if $|\nu_1\sigma_1\rangle$ and $|\nu_2\sigma_2\rangle$ belong to different IRREPs.

On the other hand, if they belong to the same IRREP $\Gamma_{\nu_1} = \Gamma_{\nu_2} = \Gamma_j$ ($j = 1$ or 5), we have to argue differently, since $\Gamma_1 \otimes \Gamma_1 = \Gamma_1$, and $\Gamma_5 \otimes \Gamma_5 \supset \Gamma_1$. Consider then the form (A29) for degenerate states ($\varepsilon_{\nu_1 \uparrow} = \varepsilon_{\nu_2 \uparrow}$). Notice that the operator $[H_{\mathrm{soz}}, p_z]$ transforms as Γ_2. The matrix element transforms as $\Gamma_j \otimes \Gamma_2 \otimes \Gamma_j$ and two cases are possible:

(a) $\Gamma_{\nu_1} = \Gamma_{\nu_2} = \Gamma_1$: $\Gamma_1 \otimes \Gamma_2 \otimes \Gamma_1 = \Gamma_2$, which yields $\langle \nu_1 \uparrow | [H_{\text{soz}}, p_z] | \nu_2 \downarrow \rangle = 0$;

(b) $\Gamma_{\nu_1} = \Gamma_{\nu_2} = \Gamma_5$: $\Gamma_5 \otimes \Gamma_2 \otimes \Gamma_5 \supset \Gamma_1$, which allows for $\langle \nu_1 \uparrow | [H_{\text{soz}}, p_z] | \nu_2 \downarrow \rangle \neq 0$.

It is easy to see, though, that the nonzero matrix element in (b) results in a negligible higher order correction, since $\frac{i}{\hbar} C \langle \nu_1 \uparrow | [H_{\text{soz}}, p_z] | \nu_2 \downarrow \rangle \propto C^2$. We shall point out that this leads to the term α_2 obtained in Ref. [42].

In summary, the matrix elements of $\langle \nu_1 \uparrow | \sigma_\mu V_z | \nu_2 \downarrow \rangle$, with $\mu = \{x, y\}$, are

(1) identically zero

(i) if $|\nu_1 \uparrow\rangle$ and $|\nu_2 \downarrow\rangle$ belong to different IRREPs;

(ii) if $\varepsilon_{\nu_1 \uparrow} = \varepsilon_{\nu_2 \uparrow}$ and $|\nu_1 \uparrow\rangle$ and $|\nu_2 \downarrow\rangle$ belong to the Γ_1 IRREP.

(2) negligible ($\propto C^2$)

(i) if $\varepsilon_{\nu_1 \uparrow} = \varepsilon_{\nu_2 \uparrow}$ and $|\nu_1 \uparrow\rangle$ and $|\nu_2 \downarrow\rangle$ belong to the Γ_5 IRREP.

Notice that, due to the spin-flip induced by the σ_μ operator acting on the matrix element, the states $|\nu_1 \uparrow\rangle$ and $|\nu_2 \uparrow\rangle$ must have the same energies, instead of $|\nu_1 \uparrow\rangle$ and $|\nu_2 \downarrow\rangle$.

The selection rules above rely on the form of our Hamiltonian given in Eqs. (A24) and (A25). This is a partially relativistic model, accounting only for the SO correction. Additionally, one could consider the scalar relativistic corrections, namely the mass-velocity $H_{mv} = \frac{p^4}{8m_0^3 c^2}$ and the Darwin $H_D = \frac{\hbar^2}{8m^2c^2} \nabla^2 V(\mathbf{r})$ terms. Both transform as Γ_1 and might contribute to the $k = 0$ diagonal matrix elements (band edges) and to the s-p_z hybridization [c_6 term in Eq. (A23)]. More importantly, these would also appear added to H_{soz} in Eq. (A29), possibly affecting the selection rule (1-ii). The mass-velocity term vanishes as $[H_{mv}, p_z] = 0$. However, the Darwin term breaks the selection rule $[H_D, p_z] \neq 0$. Nonetheless, since the latter arises from the fine structure, it scales with $H_D \propto C$, yielding again a negligible contribution $C \langle \nu_1 \uparrow | \sigma_x V_z | \nu_2 \downarrow \rangle = \frac{i}{\hbar} C \langle \nu_1 \uparrow | [H_D, p_z] | \nu_2 \uparrow \rangle \propto C^2$. This correction allows for the γ_1 and α_3 terms in Ref. [42].

b. Matrix elements

Next, let us follow the $\mathbf{k} \cdot \mathbf{p}$ approach and identify the leading order contributions for each $\mathbf{k} = 0$ term in $H_{8\times8}$ from Eq. (A23). After simplifications, these are

$$c_0 = \langle iS\uparrow | \frac{p^2}{2m_0} + V(\mathbf{r}) | iS\uparrow \rangle, \qquad \text{(A30)}$$

$$c_4 = \langle Z\uparrow | \frac{p^2}{2m_0} + V(\mathbf{r}) | Z\uparrow \rangle, \qquad \text{(A31)}$$

$$ic_6 = \langle iS\uparrow | \frac{p^2}{2m_0} + V(\mathbf{r}) | Z\uparrow \rangle, \qquad \text{(A32)}$$

$$c_3 = +\sqrt{2} C \langle X - iY\uparrow | V_y p_z - V_z p_y | Z\uparrow \rangle, \qquad \text{(A33)}$$

$$-ic_5 = +\sqrt{2} C \langle X - iY\uparrow | V_y p_z - V_z p_y | iS\uparrow \rangle. \qquad \text{(A34)}$$

Both c_6 and c_5 are nonzero due to the broken wurtzite symmetry along z (in zincblende $c_6 = c_5 = 0$). It remains to define

$c_1 = c_X + \delta c_X$ and $c_2 = c_X - \delta c_X$, in which

$$c_X = \frac{1}{2} \langle X + iY\uparrow | \frac{p^2}{2m_0} + V(\mathbf{r}) | X + iY\uparrow \rangle, \qquad \text{(A35)}$$

$$\delta c_X = \frac{1}{2} C \langle X + iY\uparrow | V_x p_y - V_y p_x | X + iY\uparrow \rangle. \qquad \text{(A36)}$$

To properly use the commutator trick introduced in Eq. (A29), it is important to keep track of the matrix form of H_0^{CC}, which includes only the z component of the SO coupling. Within this nonprimed basis, we get

$$H_0^{\text{CC}} = \begin{pmatrix} c_0 & 0 & 0 & 0 & 0 & 0 & ic_6 & 0 \\ 0 & c_0 & 0 & 0 & 0 & 0 & 0 & ic_6 \\ 0 & 0 & c_1 & 0 & 0 & 0 & 0 & 0 \\ 0 & 0 & 0 & c_1 & 0 & 0 & 0 & 0 \\ 0 & 0 & 0 & 0 & c_2 & 0 & 0 & 0 \\ 0 & 0 & 0 & 0 & 0 & c_2 & 0 & 0 \\ -ic_6 & 0 & 0 & 0 & 0 & 0 & c_4 & 0 \\ 0 & -ic_6 & 0 & 0 & 0 & 0 & 0 & c_4 \end{pmatrix}.$$

$$\text{(A37)}$$

The term c_6 is the one responsible for the s-p_z mixing [35], as it couples the states $|S\rangle$ and $|Z\rangle$.

The finite terms on the k_z block of $H_{8\times8}$ are

$$c_{16} = \frac{\hbar}{m_0} \frac{C}{\sqrt{2}} \langle X - iY\uparrow | V_y + iV_x | iS\uparrow \rangle, \qquad \text{(A38)}$$

$$ic_{18} = \frac{\hbar}{m_0} \frac{C}{\sqrt{2}} \langle X - iY\uparrow | V_y + iV_x | Z\uparrow \rangle, \qquad \text{(A39)}$$

$$c_{17} = \frac{\hbar}{m_0} \langle iS\uparrow | p_z | Z\uparrow \rangle = P_1. \qquad \text{(A40)}$$

The term c_{16} is allowed in both zincblende and wurtzite, while c_{18} only in wurtzite. However, one typically neglects these k-dependent SO terms. The term c_{17} gives us the Kane parameter P_1, also present in the CC original paper [40].

The $k_\pm$-dependent terms of $H_{8\times8}$ are given by

$$ic_8 = \frac{\hbar}{m_0} \frac{C}{2} \langle X + iY\uparrow | \sigma_y V_z | X + iY\downarrow \rangle, \qquad \text{(A41)}$$

$$ic_7 = -i \frac{\hbar C}{m_0} \langle iS\uparrow | V_z | iS\uparrow \rangle, \qquad \text{(A42)}$$

$$ic_{10} = -i \frac{\hbar C}{2m_0} \langle X - iY\uparrow | V_z | X + iY\uparrow \rangle, \qquad \text{(A43)}$$

$$ic_{12} = -i \frac{\hbar C}{m_0} \langle Z\uparrow | V_z | Z\uparrow \rangle, \qquad \text{(A44)}$$

$$c_{15} = -i \frac{\hbar C}{m_0} \langle Z\uparrow | V_z | iS\uparrow \rangle, \qquad \text{(A45)}$$

$$ic_9 = \frac{\hbar}{\sqrt{2}m_0} [\langle X - iY\downarrow | p_x + CV_y | Z\downarrow \rangle], \qquad \text{(A46)}$$

$$ic_{11} = \frac{-\hbar}{\sqrt{2}m_0} [\langle X + iY\downarrow | p_x + CV_y | Z\downarrow \rangle], \qquad \text{(A47)}$$

$$c_{13} = \frac{-\hbar}{\sqrt{2}m_0}[\langle X - iY \downarrow |p_x + CV_y|iS\downarrow\rangle], \qquad (A48)$$

$$c_{14} = \frac{-\hbar}{\sqrt{2}m_0}[\langle X + iY \downarrow |p_x + CV_y|iS\downarrow\rangle]. \qquad (A49)$$

The k-dependent SO components in c_{13} and c_{14} are usually neglected, which leads to $c_{13} = c_{14}$ for both zincblende and wurtzite. Under the same approximation, c_7, c_{10}, c_{12}, and c_{15} can be neglected. Terms $c_9 \approx -c_{11}$ can be neglected under the quasicubic assumption. As mentioned above, we cannot use the commutator trick to eliminate c_7 and c_{12}, since $|iS\uparrow\rangle$ and $|Z\uparrow\rangle$ are not eigenstates of H_0^{CC} due to the possible s-p_z mixing introduced by c_6. This is a strong motivation to change to the primed basis $|\nu'\rangle$ from Table III, which will not only eliminate c_6 through a rotation, but will also allow us to use the selection rules and the commutator trick to simplify the final model.

c. Changing basis: s-pz mixing

To eliminate the term c_6, the $|\nu'\rangle$ basis is defined by the coefficients q_s and q_z given by the eigenstates of the submatrix

$\begin{pmatrix} c_0 & ic_6 \\ -ic_6 & c_4 \end{pmatrix}$, which read

$$q_s \approx 1 - \frac{1}{2}\left(\frac{c_6}{c_0 - c_4}\right)^2, \quad q_z \approx -\left(\frac{c_6}{c_0 - c_4}\right). \qquad (A50)$$

As expected, q_s is defined by the ratio between the coupling c_6 and the gap $c_0 - c_4 = \varepsilon_{1\uparrow} - \varepsilon_{8\uparrow}$, hence $|q_z| \ll |q_s|$. The resulting primed basis $|\nu'\rangle$ diagonalizes H_0^{CC},

$$H_0^{CC'} = \begin{pmatrix} c_0' & 0 & 0 & 0 & 0 & 0 & 0 & 0 \\ 0 & c_0' & 0 & 0 & 0 & 0 & 0 & 0 \\ 0 & 0 & c_1 & 0 & 0 & 0 & 0 & 0 \\ 0 & 0 & 0 & c_1 & 0 & 0 & 0 & 0 \\ 0 & 0 & 0 & 0 & c_2 & 0 & 0 & 0 \\ 0 & 0 & 0 & 0 & 0 & c_2 & 0 & 0 \\ 0 & 0 & 0 & 0 & 0 & 0 & c_4' & 0 \\ 0 & 0 & 0 & 0 & 0 & 0 & 0 & c_4' \end{pmatrix}. \qquad (A51)$$

Let us now show the general Hamiltonian $H_{8\times8}'$ within the $|\nu'\rangle$ basis, with all symmetry allowed terms. In the next section we will select only the relevant matrix elements to build our final model. As previously done, we break the new Hamiltonian as $H_{8\times8}' = H_0' + H_z'k_z + H_\pm'k_\pm$.

The Hamiltonian H_0' reads

$$H_0' = H_0^{CC'} + \begin{pmatrix} 0 & 0 & 0 & 0 & 0 & ic_5' & 0 & 0 \\ 0 & 0 & 0 & 0 & ic_5' & 0 & 0 & 0 \\ 0 & 0 & +\delta c_X & 0 & 0 & 0 & 0 & 0 \\ 0 & 0 & 0 & +\delta c_X & 0 & 0 & 0 & 0 \\ 0 & -ic_5' & 0 & 0 & -\delta c_X & 0 & 0 & c_3' \\ -ic_5' & 0 & 0 & 0 & 0 & -\delta c_X & c_3' & 0 \\ 0 & 0 & 0 & 0 & 0 & c_3' & 0 & 0 \\ 0 & 0 & 0 & 0 & c_3' & 0 & 0 & 0 \end{pmatrix}, \qquad (A52)$$

with

$$c_0' = q_s^2 c_0 + q_z^2 c_4 - 2q_s q_z c_6 = \langle iS'\uparrow|\frac{p^2}{2m_0} + V(\mathbf{r})|iS'\uparrow\rangle, \qquad (A53)$$

$$c_4' = q_s^2 c_4 + q_z^2 c_0 + 2q_s q_z c_6 = \langle Z'\uparrow|\frac{p^2}{2m_0} + V(\mathbf{r})|Z'\uparrow\rangle, \qquad (A54)$$

$$c_3' = q_s c_3 + q_z c_5 = +\sqrt{2}C\langle X - iY\uparrow|V_y p_z - V_z p_y|Z'\uparrow\rangle, \qquad (A55)$$

$$c_5' = q_s c_5 - q_z c_3 = i\sqrt{2}C\langle X - iY\uparrow|V_y p_z - V_z p_y|iS'\uparrow\rangle. \qquad (A56)$$

All c_j' matrix elements are similar to their nonprimed c_j counterparts, except for the the replacements $S \to S'$ and $Z \to Z'$. The same is valid for the finite k_z and $k_\pm$ terms below. Indeed, for the k_z-linear terms, H_z' keeps the same form as its nonprimed counterpart in $H_{8\times8}$, with the coefficients replaced by its primed versions as

$$c_{17}' = c_{17} = \frac{\hbar}{m_0}\langle iS'\uparrow|p_z|Z'\uparrow\rangle, \qquad (A57)$$

$$c_{16}' = q_s c_{16} - q_z c_{18} = \frac{\hbar}{m_0}\frac{C}{\sqrt{2}}\langle X - iY\uparrow|V_y + iV_x|iS'\uparrow\rangle, \qquad (A58)$$

$$c_{18}' = q_s c_{18} + q_z c_{16} = -i\frac{\hbar}{m_0}\frac{C}{\sqrt{2}}\langle X - iY\uparrow|V_y + iV_x|Z'\uparrow\rangle. \qquad (A59)$$

As mentioned above, c_{16}' and c_{18}' are k-dependent SO terms that are usually neglected, while $c_{17}' = P_1$ is one of the usual Kane parameters.

The change of basis truly pays off due to the simplifications on $H'_\pm$. We can now use the commutator trick to further eliminate

$$ic'_7 = -i\frac{\hbar C}{m_0}\langle iS'\uparrow|V_z|iS'\uparrow\rangle = 0,$$

$$ic'_{12} = -i\frac{\hbar C}{m_0}\langle Z'\uparrow|V_z|Z'\uparrow\rangle = 0. \tag{A60}$$

Therefore we get

$$H'_\pm = \begin{pmatrix} 0 & 0 & c'^+_{13} & 0 & -c'^-_{14} & 0 & 0 & -c'^-_{15} \\ 0 & 0 & 0 & -c'^-_{13} & 0 & c'^+_{14} & c'^+_{15} & 0 \\ c'^-_{13} & 0 & 0 & 0 & 0 & 0 & ic'^-_9 & 0 \\ 0 & -c'^+_{13} & 0 & 0 & 0 & 0 & 0 & ic'^-_9 \\ -c'^+_{14} & 0 & 0 & 0 & 0 & -ic'^-_{10} & -ic'^-_{11} & 0 \\ 0 & c'^-_{14} & 0 & 0 & +ic'^+_{10} & 0 & 0 & ic'^-_{11} \\ 0 & c'^-_{15} & -ic'^+_9 & 0 & +ic'^+_{11} & 0 & 0 & 0 \\ -c'^+_{15} & 0 & 0 & -ic'^+_9 & 0 & -ic'^+_{11} & 0 & 0 \end{pmatrix}, \tag{A61}$$

with $c'_{10} = c_{10}$, and

$$ic'_9 = \frac{\hbar}{\sqrt{2}m_0}[\langle X - iY\downarrow|p_x|Z'\downarrow\rangle + C\langle X - iY\downarrow|V_y|Z'\downarrow\rangle], \tag{A62}$$

$$ic'_{11} = \frac{-\hbar}{\sqrt{2}m_0}[\langle X + iY\downarrow|p_x|Z'\downarrow\rangle + C\langle X + Y\downarrow|V_y|Z'\downarrow\rangle], \tag{A63}$$

$$c'_{13} = \frac{-\hbar}{\sqrt{2}m_0}[\langle X - iY\downarrow|p_x|iS'\downarrow\rangle + C\langle X - iY\downarrow|V_y|iS'\downarrow\rangle], \tag{A64}$$

$$c'_{14} = \frac{-\hbar}{\sqrt{2}m_0}[\langle X + iY\downarrow|p_x|iS'\downarrow\rangle + C\langle X + iY\downarrow|V_y|iS'\downarrow\rangle], \tag{A65}$$

$$c'_{15} = -i\frac{\hbar C}{m_0}\langle Z'\uparrow|V_z|iS'\uparrow\rangle. \tag{A66}$$

d. Approximations and final model

Up to this point, the results above are exactly derived from the symmetry constraints and selection rules from Appendix A 4 a. In the following we introduce the approximations that lead to the final model $H^{CC'}_{8\times8}$ shown in Eq. (7) of the main text.

If one is interested in the electron bands, it is usual to neglect the k-dependent SO terms, which only contribute in high orders to the Löwdin partitioning. This approximation eliminates $c'_{10} \approx c'_{15} \approx c'_{16} \approx c'_{18} \approx 0$. Moreover, it allow us to neglect the SO contribution in c'_9, c'_{11}, c'_{13}, c'_{14}, which yields $c'_{13} \approx c'_{14} \equiv -P_2/\sqrt{2}$ as a Kane parameter, while $c'_9 \approx -c'_{11} \approx 0$ within the quasicubic approximation. We have already defined $c'_{17} = P_1$. For the $k = 0$ terms, it follows that $c'_0 = E_c, c_X = E_v + \Delta_1, \delta c_X = \Delta_2, c'_4 = E_v, c'_3 = \sqrt{2}\Delta_3$, and $c'_5 = -\sqrt{2}\Delta_{sz}$. By setting $E_c = 0$ (energy reference) and $E_v + \Delta_1 + \Delta_2 = -E_g$, we have $c'_0 = 0$, $c'_1 = -E_g$, $c'_2 = -E_g - 2\Delta_2$, and $c'_4 = -E_g - \Delta_1 - \Delta_2$. Under these assumptions, the $H'_{8\times8}$ from the previous section yields our model $H^{CC'}_{8\times8}$ shown in Eq. (7).

e. Remarks on Δ_3 and Δ_{sz}

For most of the terms above, the difference between the primed c'_j and nonprimed c_j matrix elements is nearly irrelevant. However, it is worth noting that this is not the case for the terms c'_3 and c'_5.

We have shown that $c'_3 = q_s c_3 + q_z c_5$. Let us assume that the s-p_z hybridization is small, it follows that $q_z \ll q_s$ and we can take $q_s \approx 1$. The dominant contribution is $c'_3 \approx c_3$, which gives us

$$\Delta_3 = \frac{c'_3}{\sqrt{2}} = C\langle X - iY\uparrow|V_y p_z - V_z p_y|Z'\uparrow\rangle$$

$$\approx \frac{c_3}{\sqrt{2}} = C\langle X - iY\uparrow|V_y p_z - V_z p_y|Z\uparrow\rangle. \tag{A67}$$

The case for the term $c'_5 = -\sqrt{2}\Delta_{sz}$ is more delicate. The s-p_z hybridization leads to $c'_5 = q_s c_5 - q_z c_3$, which may be written as

$$\Delta_{sz} = -\frac{q_s c_5 - q_z c_3}{\sqrt{2}} = -q_s\frac{c_5}{\sqrt{2}} + q_z\Delta_3$$

$$= C[-iq_s\langle X - iY\uparrow|V_y p_z - V_z p_y|iS\uparrow\rangle$$

$$+ q_z\langle X - iY\uparrow|V_y p_z - V_z p_y|Z\uparrow\rangle]. \tag{A68}$$

Notice that both matrix elements above arise from the k-independent SO term and are nearly identical, except for the change $|iS\uparrow\rangle \leftrightarrow |Z\uparrow\rangle$. Therefore, we may wonder which contribution prevails. One can argue that the first matrix element (arising from c_5, with $|iS\uparrow\rangle$) is small under the quasicubic approximation. However, it multiplies $q_s \approx 1$. On the other hand, the second term (arising from Δ_3, with $|Z\uparrow\rangle$) is finite

TABLE IV. Real band edges λ_i (E_i) with $i = e, A, B, C$ and corresponding eigenfunctions $u_i \equiv u_{i0}(\mathbf{r})$ of H_0^{diag} at $\mathbf{k} = 0$. The relevant constants A_{λ_i}, c_1, c_2, E_{AB}, and E_{AC} are defined in Eqs. (B3) and (B4). The eigenergy λ_i (E_i) corresponds to the band edge energy with (without) the s-p_z mixing contribution. The difference between λ_i and E_i is less than 10^{-3} meV.

E_i	u_i
$\lambda_e \simeq E_e$	$\|u_1\rangle = A_{\lambda_e}\big[iS'\uparrow\rangle - \big(\frac{c_1^2}{E_g+E_{AB}+\lambda_e} + \frac{c_2^2}{E_g+E_{AC}+\lambda_e}\big)i\Delta_{\text{sz}}(\|X\downarrow\rangle + i\|Y\downarrow\rangle) + i\sqrt{2}c_1c_2\Delta_{\text{sz}}\big(\frac{1}{E_g+E_{AB}+\lambda_e} - \frac{1}{E_g+E_{AC}+\lambda_e}\big)\|Z'\uparrow\rangle\big]$
$\lambda_e \simeq E_e$	$\|u_2\rangle = A_{\lambda_e}\big[iS'\downarrow\rangle + \big(\frac{c_1^2}{E_g+E_{AB}+\lambda_e} + \frac{c_2^2}{E_g+E_{AC}+\lambda_e}\big)i\Delta_{\text{sz}}(\|X\uparrow\rangle - i\|Y\uparrow\rangle) + i\sqrt{2}c_1c_2\Delta_{\text{sz}}\big(\frac{1}{E_g+E_{AB}+\lambda_e} - \frac{1}{E_g+E_{AC}+\lambda_e}\big)\|Z'\downarrow\rangle\big]$
$\lambda_A \simeq E_A$	$\|u_3\rangle = -\frac{1}{\sqrt{2}}(\|X\uparrow\rangle + i\|Y\uparrow\rangle)$
$\lambda_A \simeq E_A$	$\|u_4\rangle = \frac{1}{\sqrt{2}}(\|X\downarrow\rangle - i\|Y\downarrow\rangle)$
$\lambda_B \simeq E_B$	$\|u_5\rangle = A_{\lambda_B}\big[iS'\uparrow\rangle - \big(\frac{c_1^2}{E_g+E_{AB}+\lambda_B} + \frac{c_2^2}{E_g+E_{AC}+\lambda_B}\big)i\Delta_{\text{sz}}(\|X\downarrow\rangle + i\|Y\downarrow\rangle) + i\sqrt{2}c_1c_2\Delta_{\text{sz}}\big(\frac{1}{E_g+E_{AB}+\lambda_B} - \frac{1}{E_g+E_{AC}+\lambda_B}\big)\|Z'\uparrow\rangle\big]$
$\lambda_B \simeq E_B$	$\|u_6\rangle = A_{\lambda_B}\big[iS'\downarrow\rangle + \big(\frac{c_1^2}{E_g+E_{AB}+\lambda_B} + \frac{c_2^2}{E_g+E_{AC}+\lambda_B}\big)i\Delta_{\text{sz}}(\|X\uparrow\rangle - i\|Y\uparrow\rangle) + i\sqrt{2}c_1c_2\Delta_{\text{sz}}\big(\frac{1}{E_g+E_{AB}+\lambda_B} - \frac{1}{E_g+E_{AC}+\lambda_B}\big)\|Z'\downarrow\rangle\big]$
$\lambda_C \simeq E_C$	$\|u_7\rangle = A_{\lambda_C}\big[iS'\uparrow\rangle - \big(\frac{c_1^2}{E_g+E_{AB}+\lambda_C} + \frac{c_2^2}{E_g+E_{AC}+\lambda_C}\big)i\Delta_{\text{sz}}(\|X\downarrow\rangle + i\|Y\downarrow\rangle) + i\sqrt{2}c_1c_2\Delta_{\text{sz}}\big(\frac{1}{E_g+E_{AB}+\lambda_C} - \frac{1}{E_g+E_{AC}+\lambda_C}\big)\|Z'\uparrow\rangle\big]$
$\lambda_C \simeq E_C$	$\|u_8\rangle = A_{\lambda_C}\big[iS'\downarrow\rangle + \big(\frac{c_1^2}{E_g+E_{AB}+\lambda_C} + \frac{c_2^2}{E_g+E_{AC}+\lambda_C}\big)i\Delta_{\text{sz}}(\|X\uparrow\rangle - i\|Y\uparrow\rangle) + i\sqrt{2}c_1c_2\Delta_{\text{sz}}\big(\frac{1}{E_g+E_{AB}+\lambda_C} - \frac{1}{E_g+E_{AC}+\lambda_C}\big)\|Z'\downarrow\rangle\big]$

even in zincblende, but multiplies $|q_z| \ll |q_s|$. Thus, it is not possible to define the dominant term *a priori*.

Typically, one argues in favor of the quasicubic approximation to parametrize $\Delta_{\text{sz}} \approx q_z \Delta_3$ in terms of Δ_3, using q_z as a free fitting parameter. However, the analysis above shows that this is not a good and systematic approach. Instead, we consider that it is better to keep Δ_{sz} itself as an independent parameter for wurtzite crystals. Notice that Δ_{sz} naturally vanishes in zincblende, for which $c_5 = q_z = 0$.

APPENDIX B: KANE MODEL: DIAGONAL BASIS

Here we obtain the real band edges and the corresponding basis set $u_{io}(\mathbf{r})$ that diagonalizes the Hamiltonian $H_0^{\text{diag}} = H_0^{\text{CC}'} + H_{\text{sox}} + H_{\text{soy}}$ at $k = 0$.

1. Unstrained case

The actual band edges and corresponding basis functions $u_{i0}(\mathbf{r})$ without strain can be obtained by diagonalizing the corresponding CC'-basis Kane model [Eqs. (7)] at $\mathbf{k} = 0$. The energy differences between the band edges, shown in Fig. 1(a) (neglecting Δ_{sz}), are given by

$$E_{AB} = \tfrac{1}{2}(\Delta_{\text{cr}} + 3\Delta_2) - \tfrac{1}{2}\sqrt{(\Delta_{\text{cr}} - \Delta_2)^2 + 8\Delta_3^2}, \quad \text{(B1)}$$

$$E_{AC} = \tfrac{1}{2}(\Delta_{\text{cr}} + 3\Delta_2) + \tfrac{1}{2}\sqrt{(\Delta_{\text{cr}} - \Delta_2)^2 + 8\Delta_3^2}, \quad \text{(B2)}$$

$$E_{BC} = E_{AC} - E_{AB} = \sqrt{(\Delta_{\text{cr}} - \Delta_2)^2 + 8\Delta_3^2}. \quad \text{(B3)}$$

The diagonal basis $u_{i0}(\mathbf{r})$ shown in Table IV has the following normalization constants

$$A_{\lambda_i} = 1\Big/ \sqrt{1 + \frac{2c_1^2\Delta_{\text{sz}}^2}{(E_g + E_{AB} + \lambda_i)^2} + \frac{2c_2^2\Delta_{\text{sz}}^2}{(E_g + E_{AC} + \lambda_i)^2}}, \tag{B4}$$

where A_{λ_i} ($i = e, A, B,$ and C) and

$$c_1 = \frac{E_{AC} - 2\Delta_2}{\sqrt{(E_{AC} - 2\Delta_2)^2 + 2\Delta_3^2}},$$

$$c_2 = \frac{\sqrt{2}\Delta_3}{\sqrt{(E_{AC} - 2\Delta_2)^2 + 2\Delta_3^2}}, \tag{B5}$$

with $c_1^2 + c_2^2 = 1$. The eigenvalue of H_0^{diag} λ_i corresponds to the energy of the real band edges. If we focus only on the band structure, a good approximation is to neglect the s-p_z mixing, which yields a correction to the band edges of less than 10^{-3} meV compared to the real ones. By taking the conduction band as the energy origin, namely $\lambda_e = 0$, we have

$$\lambda_A \simeq E_A = -E_g, \tag{B6}$$

$$\lambda_B \simeq E_B = -E_g - E_{AB}, \tag{B7}$$

$$\lambda_C \simeq E_C = -E_g - E_{AC}, \tag{B8}$$

which directly maps to the band description in Fig. 1(a) (solid curves). Note that, to obtain the basis functions shown in Table IV, we need to perform an exact numerical calculation of the band edge energies.

The 8×8 matrix Hamiltonian in the diagonal basis is given by

$$
H_0^{\text{diag}} = \frac{p^2}{2m_0} + \begin{pmatrix}
\lambda_e & i\alpha_{\text{bulk}}k_- & -A_{\lambda_e}\frac{P_2}{\sqrt{2}}k_+ & 0 & if_{\lambda_e\lambda_B}k_- & \frac{i}{2}\{g_{\lambda_e\lambda_B},k_z\} & if_{\lambda_e\lambda_C}k_- & \frac{i}{2}\{g_{\lambda_e\lambda_C},k_z\} \\
-i\alpha_{\text{bulk}}k_+ & \lambda_e & 0 & A_{\lambda_e}\frac{P_2}{\sqrt{2}}k_- & \frac{i}{2}\{g_{\lambda_e\lambda_B},k_z\} & -if_{\lambda_e\lambda_B}k_+ & \frac{i}{2}\{g_{\lambda_e\lambda_C},k_z\} & -if_{\lambda_e\lambda_C}k_+ \\
-A_{\lambda_e}\frac{P_2}{\sqrt{2}}k_- & 0 & \lambda_A & 0 & 0 & 0 & 0 & 0 \\
0 & A_{\lambda_e}\frac{P_2}{\sqrt{2}}k_+ & 0 & \lambda_A & 0 & 0 & 0 & 0 \\
-if_{\lambda_e\lambda_B}k_+ & -\frac{i}{2}\{g_{\lambda_e\lambda_B},k_z\} & 0 & 0 & \lambda_B & 0 & 0 & 0 \\
-\frac{i}{2}\{g_{\lambda_e\lambda_B},k_z\} & if_{\lambda_e\lambda_B}k_- & 0 & 0 & 0 & \lambda_B & 0 & 0 \\
-if_{\lambda_e\lambda_C}k_+ & -\frac{i}{2}\{g_{\lambda_e\lambda_C},k_z\} & 0 & 0 & 0 & 0 & \lambda_C & 0 \\
-\frac{i}{2}\{g_{\lambda_e\lambda_C},k_z\} & if_{\lambda_e\lambda_C}k_- & 0 & 0 & 0 & 0 & 0 & \lambda_C
\end{pmatrix},
$$

$$\text{(B9)}$$

with $\{:,:\}$ denoting the anticommutator. Here we neglected containing second-order terms in Δ_{sz} and the matrix elements within the valence band. These would give rise to negligible higher order contributions proportional to Δ_{sz}. The coefficient α_{bulk} is the bulk Rashba parameter,

$$
\alpha_{\text{bulk}} = 2A_{\lambda_e}^2 P_2 \Delta_{\text{sz}} \left(\frac{c_1^2}{E_g + E_{AB} + \lambda_e} + \frac{c_2^2}{E_g + E_{AC} + \lambda_e} \right). \tag{B10}
$$

If we properly expand the expression above, we can recover the result in Eq. (27).

The parameters $f_{\lambda_e\lambda_{i=B,C}}$ and $g_{\lambda_e\lambda_{i=B,C}}$ in Eq. (B9) are defined as

$$
f_{\lambda_e\lambda_i} = A_{\lambda_e}A_{\lambda_i}P_2\Delta_{\text{sz}}\left[c_1^2\left(\frac{1}{E_g + E_{AB} + \lambda_e} + \frac{1}{E_g + E_{AB} + \lambda_i} \right) + c_2^2\left(\frac{1}{E_g + E_{AC} + \lambda_e} + \frac{1}{E_g + E_{AC} + \lambda_i} \right) \right] \tag{B11}
$$

and

$$
g_{\lambda_e\lambda_i} = \sqrt{2}A_{\lambda_e}A_{\lambda_i}c_1c_2P_1\Delta_{\text{sz}}\left[\left(\frac{1}{E_g + E_{AB} + \lambda_i} - \frac{1}{E_g + E_{AB} + \lambda_e} \right) - \left(\frac{1}{E_g + E_{AC} + \lambda_i} - \frac{1}{E_g + E_{AC} + \lambda_e} \right) \right]. \tag{B12}
$$

Note that for calculating the parameters above, we should use the eigenvalues of (B9) obtained numerically.

In Table V we show the relation between the band edges and quantum well offsets of the CC′ and the diagonal basis sets. For simplicity, here we use the superscript CC′ to refer to the quantities in Sec. II.

2. Strained case

In the presence of strain, u_{i0} is obtained by diagonalizing the strained CC′-basis Kane Hamiltonian (see Sec. II B 2). Therefore, the diagonal basis set is strain dependent.

To construct the Kane model using the diagonal basis in the presence of strain, we need to know how the band edges change compared to the unstrained case. One can obtain these by numerically diagonalizing the Hamiltonian. Here, however, we show the analytical expressions within the approximation of neglecting the s-p_z mixing, since its energy correction is negligibly small. The band edge shift due to strain at the Γ point is schematically shown in Fig. 1(a) (dashed curves), where we have $E_e^{\text{s}} = E_e + a_{c_1}\varepsilon_{zz} + a_{c_2}(\varepsilon_{xx} + \varepsilon_{yy})$, $E_A^{\text{s}} = E_A + S_1 + S_2$, $E_B^{\text{s}} = E_A^{\text{s}} - E_{AB}^{\text{s}}$, and $E_C^{\text{s}} = E_A^{\text{s}} - E_{AC}^{\text{s}}$. The energy

differences between the valence bands in the presence of strain E_{AB}^{s}, E_{AC}^{s}, and E_{BC}^{s} read

$$
E_{AB}^{\text{s}} = \frac{1}{2}(\Delta_{\text{cr}} + 3\Delta_2 + S_2) - \frac{1}{2}\sqrt{(\Delta_{\text{cr}} - \Delta_2 + S_2)^2 + 8\Delta_3^2}, \tag{B13}
$$

$$
E_{AC}^{\text{s}} = \frac{1}{2}(\Delta_{\text{cr}} + 3\Delta_2 + S_2) + \frac{1}{2}\sqrt{(\Delta_{\text{cr}} - \Delta_2 + S_2)^2 + 8\Delta_3^2}, \tag{B14}
$$

$$
E_{BC}^{\text{s}} = E_{AC}^{\text{s}} - E_{BC}^{\text{s}} = \sqrt{(\Delta_{\text{cr}} - \Delta_2 + S_2)^2 + 8\Delta_3^2}. \tag{B15}
$$

We can directly compare the expressions above with the unstrained case [Eqs. (B1)–(B3)] and see the corrections due to strain.

The Kane Hamiltonian in the presence of strain is again similar to that of the unstrained case, with the band parameters in Eq. (B9) being replaced by the strained parameters given above.

APPENDIX C: FOLDING DOWN APPROACH

For an arbitrary $n \times n$ matrix Hamiltonian, one can always write the corresponding Schrödinger equation in the compact

TABLE V. Relation between the bulk band edges E_i [Fig. 1(a)] and quantum well offsets δ_i [Fig. 1(b)], of the CC′ and diagonal basis sets. The notation refers to the unstrained case; the strained case can be straightforwardly obtained. The superscripts "w" and "b" stand for well and barrier, respectively. For the expressions of energy separations E_{AB} and E_{AC} in each basis set, see Eqs. (9) and (B1)–(B3).

$E_e^{CC'} = E_e$	$E_A^{CC'} = E_A$	$E_g^{CC'} = E_g$
$E_B^{CC'} = E_B + E_{AB} - E_{AB}^{CC'}$	$E_C^{CC'} = E_C + E_{AC} - E_{AC}^{CC'}$	
$\delta_e^{CC'} = \delta_e$	$\delta_B^{CC'} = \delta_B + \left(E_{AB}^{CC'} - E_{AB}\right)^b - \left(E_{AB}^{CC'} - E_{AB}\right)^w$	
$\delta_A^{CC'} = \delta_A$	$\delta_C^{CC'} = \delta_C + \left(E_{AC}^{CC'} - E_{AC}\right)^b - \left(E_{AC}^{CC'} - E_{AC}\right)^w$	

form

$$\begin{pmatrix} H_P & H_{PQ} \\ H_{PQ}^\dagger & H_Q \end{pmatrix} \begin{pmatrix} \Phi_P \\ \Phi_Q \end{pmatrix} = E \begin{pmatrix} \Phi_P \\ \Phi_Q \end{pmatrix}, \tag{C1}$$

where H_P and H_Q are two subsets of the original matrix, H_{PQ} describes the coupling between these subspaces, and Φ_P and Φ_Q are the corresponding eigenspinors. Here, as shown below, we are interested in the subspace P.

We can use the so-called folding down approach to rewrite Eq. (C1) as

$$\mathcal{H}_P(E)\Phi_P = E\Phi_P, \tag{C2}$$

with

$$\mathcal{H}_P(E) = [H_P + H_{PQ}(E - H_Q)^{-1}H_{PQ}^\dagger]. \tag{C3}$$

Note that $\mathcal{H}_P(E)$ is energy dependent, which makes Eq. (C2) not a *real* Schrödinger-type equation.

To ensure norm conservation, we build a new spinor Φ_P',

$$\Phi_P' = \Omega\Phi_P, \quad \Omega = \sqrt{1 + H_{PQ}\frac{1}{(E - H_Q)^2}H_{PQ}^\dagger}. \tag{C4}$$

By inserting Φ_P' into Eq. (C2) and multiplying the resulting equation from the left by Ω^{-1}, we arrive at

$$\Omega^{-1}\mathcal{H}_P(E)\Omega^{-1}\Phi_P' = E\Omega^{-2}\Phi_P'. \tag{C5}$$

From Eq. (C5) we obtain

$$\mathcal{H}_P'(E)\Phi_P' = E\Phi_P', \tag{C6}$$

with

$$\mathcal{H}_P'(E) = [\Omega^{-1}\mathcal{H}_P(E)\Omega^{-1} + E(I - \Omega^{-2})], \tag{C7}$$

where I is the identity matrix, which has the same dimension of the subspace P. From Eq. (C6), it is possible to arrive at a real Schrödinger-type equation, i.e., $\mathcal{H}_P'(E) \to \mathcal{H}_P'$ energy independent, by performing a power expansion of $(E - H_Q)^{-1}$ up to the second order in the energy E.

By using the procedure described above, we obtain exactly the same result as in Eqs. (30)–(36).

APPENDIX D: $k \cdot p$ INTERACTION WITHIN THE VALENCE BAND SUBSPACE

In Sec. III B we have derived an expression for the Rashba coupling, Eq. (37), taking into account only $k \cdot p$ terms between conduction and valence bands. Here we extend our analysis to include the $k \cdot p$ interaction within the valence bands. We then use the Löwdin perturbation theory (or equivalently the folding down approach) to obtain a 2×2 Hamiltonian for the conduction electrons that includes additional terms to the Rashba and Dresselhaus SO couplings. As we shall see below, these additional Rashba terms are small compared to those in the main text. As for the Dresselhaus terms, they also give a negligible contribution.

The 6×6 Hamiltonian (CC′ basis) for the p valence band including the $k \cdot p$ interaction within its subspace is given by

$$H_v = \frac{p^2}{2m_0} + \begin{pmatrix} -E_g + V_A(z) & 0 & 0 & 0 & \frac{iQ}{\sqrt{2}}k_- & 0 \\ 0 & -E_g + V_A(z) & 0 & 0 & 0 & -\frac{iQ}{\sqrt{2}}k_+ \\ 0 & 0 & -E_g - E_{AB} + V_B(z) & 0 & -\frac{iQ}{\sqrt{2}}k_+ & \sqrt{2}\Delta_3 \\ 0 & 0 & 0 & -E_g - E_{AB} + V_B(z) & \sqrt{2}\Delta_3 & \frac{iQ}{\sqrt{2}}k_- \\ -\frac{iQ}{\sqrt{2}}k_+ & 0 & \frac{iQ}{\sqrt{2}}k_- & \sqrt{2}\Delta_3 & -E_g - E_{AC} + V_C(z) & 0 \\ 0 & \frac{iQ}{\sqrt{2}}k_- & \sqrt{2}\Delta_3 & -\frac{iQ}{\sqrt{2}}k_+ & 0 & -E_g - E_{AC} + V_C(z) \end{pmatrix}, \tag{D1}$$

with Q being defined as $Q = -(i\hbar/m_0)\langle Z'|p_x|X\rangle = -(i\hbar/m_0)\langle Z'|p_y|Y\rangle$. The additional Rashba terms arising from the $k \cdot p$ coupling inside the valence band subspace read

$$H_R^Q = \eta_Q(z)(\sigma_x k_y - \sigma_y k_x), \tag{D2}$$

with

$$\eta_Q(z) = \frac{P_1 Q \Delta_{\text{sz}}}{(E_g + 2\Delta_2)^2 (E_g + \Delta_1 + \Delta_2)} \frac{dV_B(z)}{dz} + \frac{P_1 Q \Delta_{\text{sz}}}{(E_g + 2\Delta_2)(E_g + \Delta_1 + \Delta_2)^2} \frac{dV_C(z)}{dz} + \frac{4\Delta_{\text{sz}}^2 \Delta_3 Q}{(E_g + 2\Delta_2)^2 (E_g + \Delta_1 + \Delta_2)},$$

$$(D3)$$

where one can see that these terms also depend on the s-p_z mixing, i.e., Δ_{sz}. The first two terms in the equation above describe SIA Rashba terms. By assuming that the Kane parameters P_2 and Q are comparable, we find that the strength of these contributions (after taking an expectation value using a proper self-consistent wave function) is around one tenth of that obtained from $\eta_{\text{SIA}}(z)$ [Eq. (41)] in the main text. The last term in (D3) is an additional BIA Rashba contribution and has also an negligible expectation value as compared to the $\alpha_{\text{bulk}}^{\text{BIA}}$ in Eq. (27).

We also obtain extra BIA Dresselhaus terms (arising from the $\boldsymbol{k} \cdot \boldsymbol{p}$ coupling inside the valence sector) proportional to the parameter Q. The BIA Dresselhaus Hamiltonian reads

$$H_D = \gamma \left(-b \frac{d^2}{dz^2} - k_\parallel^2 \right) (\sigma_x k_y - \sigma_y k_x), \quad (D4)$$

with the coefficients

$$\gamma = \gamma_1 + \gamma_2 \quad (D5)$$

and

$$b = b_1 + b_2 \quad (D6)$$

defined in terms of

$$\gamma_1 = -\frac{P_2^3 \Delta_{\text{sz}}}{E_g + E_{AB}} \left[\frac{1}{E_g^2} + \frac{2}{(E_g + E_{AB})^2} + \frac{1}{E_g(E_g + E_{AB})} \right], \quad (D7)$$

$$\gamma_2 = \frac{P_2 Q (Q\Delta_{\text{sz}} + P_2 \Delta_3)}{(E_g + E_{AB})(E_g + E_{AC})} \left(\frac{1}{E_g} + \frac{1}{E_g + E_{AB}} \right), \quad (D8)$$

$$b_1 = -\frac{2P_1^2 P_2 \Delta_{\text{sz}}}{\gamma (E_g + E_{AB})(E_g + E_{AC})} \left(\frac{1}{E_g + E_{AC}} + \frac{1}{E_g + E_{AB}} \right), \quad (D9)$$

and

$$b_2 = \frac{2P_1^2 Q \Delta_3}{\gamma (E_g + E_{AB})(E_g + E_{AC})^2}. \quad (D10)$$

The constants γ_1 and γ_2 describe the bulk Dresselhaus coefficients. As mentioned in the main text, the former arises entirely from the s-p_z mixing and does not depend on Q and the latter is determined by Q. It is worth mentioning that the s-p_z mixing also partially contributes to γ_2 [see Eq. (D8)]. The parameter b implies the nonequivalence between the c axis oriented z direction and the x-y plane.

We must emphasize that the Dresselhaus term here was obtained within the eight-band model (s-conduction and $\boldsymbol{p}$-valence bands). This is in contrast to the zincblende structure, in which the Dresselhaus term is associated with the coupling between the $\boldsymbol{p}$-valence and $\boldsymbol{p}$-conduction bands.

On the other hand, from Eqs. (D5)–(D10) we evaluate $\gamma \sim 0.08$ meV Å^3 and $b \sim 0.01$, whose values are much smaller than the semiempirical values $\gamma \sim 0.32$ meV Å^3 and $b \sim 4.0$ [24] and the experimental results in Ref. [41]. The work by Fu and Wu indicates that remote bands may generate the main contribution to the Dresselhaus SO coupling. Further studies to obtain a full expression in terms of the parameters of the remote bands are needed. As mentioned in the main text, in our self-consistent simulations we treat the coefficients γ and b in Eq. (D4) as semiempirical parameters.

APPENDIX E: TOTAL HARTREE POTENTIAL

The total Hartree potential, given in Eq. (20) of the main text, has several contributions (these arise from different charge densities): V_{elect}, V_{int}, V_d, and V_g. Here we explicitly show how to determine each one of these terms from the Poisson equation.

1. Pure Hartree potential: V_{elect}

The pure Hartree potential V_{elect} is obtained by solving

$$\frac{d^2}{dz^2} V_{\text{elect}}(z) = \frac{e}{\epsilon_0 \epsilon_r} \rho_e(z), \quad (E1)$$

together with the Dirichlet boundary conditions $V_{\text{elect}}(\pm L) = 0$, where $\pm L$ are the end points of our system (see Fig. 8) and $e > 0$ is the elementary charge. The parameter $\rho_e(z)$ corresponds to the electronic charge density and reads

$$\rho_e(z) = -\frac{2e}{A} \sum_{\nu, k_\parallel} |e^{i\mathbf{k}_\parallel \cdot \mathbf{r}} \psi_\nu(z)|^2 f(\mathcal{E}_{k_\parallel \nu}), \quad (E2)$$
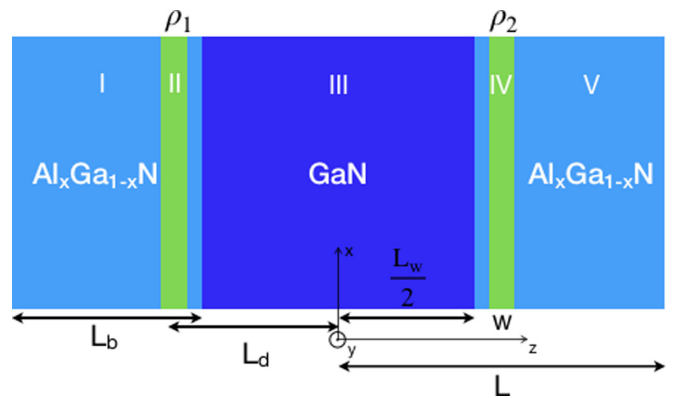

FIG. 8. Schematic of a GaN/Al$_x$Ga$_{1-x}$N quantum well grown along the $z || [0001]$ direction. The well region and the two symmetric barriers have widths $L_w = 10$ nm and $L_b = 7$ nm, respectively. Regions II and IV correspond to two doping layers of densities ρ_1 and ρ_2 and width w, symmetrically located at $L_d = 6$ nm from the center of the well. The total width of the system is $2L$.

with A the area of the electron gas in the xy plane (normalizing constant) and $f(\mathcal{E}_{k\parallel\nu})$ the Fermi-Dirac distribution. More explicitly,

$$\rho_e(z) = -\frac{em^*}{\pi\hbar^2}k_B T \sum_\nu |\psi_\nu(z)|^2 \ln\left[1 + e^{(\mu - \varepsilon_\nu)/k_B T}\right], \quad \text{(E3)}$$

in which k_B is the Boltzmann constant, T is the temperature, and μ is the chemical potential.

We shall point that $\rho_e(z)$ in Eq. (E1) depends on the wave functions $\psi_\nu(z)$ [see Eq. (E3)], which were obtained by solving the Schrödinger equation for the quantum well (31). This equation depends on the total potential $V_e(z)$, which in turn has $V_{\text{elect}}(z)$ as one of its contributions. Hence, to determine $\psi_\nu(z)$ and $\rho_e(z)$, we self-consistently solve Schrödinger and Poisson's equations for the total charge density (see next sections for the other charge density contributions).

2. Internal potential: V_{int}

The internal potential V_{int} due to the built-in electric field is written as

$$V_{\text{int}}(z) = e\int_{-L}^{z} E_{\text{int}}(z')dz', \quad \text{(E4)}$$

where $E_{\text{int}}(z')$ can be either E_w or E_b given in Eq. (16) (periodic boundary conditions) or (17) (neutral surface charges). The solutions in terms of the fields read

$$V_{\text{int}}(z) = \begin{cases} eE_b(z+L), & -L \leqslant z \leqslant -L_w/2, \\ eE_b\left(L - \frac{L_w}{2}\right) + eE_w\left(z + \frac{L_w}{2}\right), & -L_w/2 \leqslant z \leqslant L_w/2, \\ eE_b(z + L - L_w) + eE_w L_w, & L_w/2 \leqslant z \leqslant L. \end{cases} \quad \text{(E5)}$$

3. Doping + external gate potentials: $V_{\text{d}} + V_{\text{g}}$

These two contributions can be obtained by solving the Poisson equation + boundary conditions in each region (I–V) of our system (Fig. 8) [20].

For the doping potential V_d we have

$$\frac{d^2}{dz^2}V_d(z) = \frac{e^2}{\epsilon_0\epsilon_r} \begin{cases} 0, & -L \leqslant z \leqslant -L_d, & \text{(I)} \\ \rho_1, & -L_d \leqslant z \leqslant -L_d + w, & \text{(II)} \\ 0, & -L_d + w \leqslant z \leqslant L_d - w, & \text{(III)} \\ \rho_2, & L_d - w \leqslant z \leqslant L_d, & \text{(IV)} \\ 0, & L_d \leqslant z \leqslant L. & \text{(V)} \end{cases} \quad \text{(E6)}$$

where $\rho_{1,2}$ are the doping densities. The solutions to the equations above are given by

$$V_d(z) = \begin{cases} a_1 z + a_2, & \text{(I)} \\ \frac{e^2\rho_1}{2\epsilon_0\epsilon_r}z + a_3 z + a_4, & \text{(II)} \\ a_5 z + a_6, & \text{(III)} \\ \frac{e^2\rho_2}{2\epsilon_0\epsilon_r}z + a_7 z + a_8, & \text{(IV)} \\ a_9 z + a_{10}. & \text{(V)} \end{cases} \quad \text{(E7)}$$

The coefficients a_i, $i = 1, \ldots, 10$, are obtained by imposing the continuity of V_d and its derivative. In addition, we consider the Dirichlet boundary conditions $V_d(\pm L) = 0$. The explicit expressions for these constants can be found in Appendix B of Ref. [20].

For the external gate potential V_g, we solve

$$\frac{d^2}{dz^2}V_g(z) = 0, \quad -L \leqslant z \leqslant L, \quad \text{(E8)}$$

with the Dirichlet boundary conditions $V_g(-L) = V_1$ and $V_g(L) = V_2$, where $V_{1,2}$ are the external gates at the end points $\pm L$. We then obtain

$$V_g(z) = -\frac{(V_1 - V_2)}{2L}z + \frac{(V_1 + V_2)}{2}. \quad \text{(E9)}$$

[1] D. Awschalom, D. Loss, and N. Samarth, *Semiconductor Spintronics and Quantum Computation* (Springer, New York, 2002).

[2] I. Žutić, J. Fabian, and S. D. Sarma, Rev. Mod. Phys. **76**, 323 (2004).

[3] C. L. Kane and E. J. Mele, Phys. Rev. Lett. **95**, 226801 (2005).

[4] B. A. Bernevig, T. L. Hughes, and S. C. Zhang, Science **314**, 1757 (2006).

[5] J. Alicea, Phys. Rev. B **81**, 125318 (2010).

[6] R. M. Lutchyn, J. D. Sau, and S. Das Sarma, Phys. Rev. Lett. **105**, 077001 (2010).

[7] Y. Oreg, G. Refael, and F. von Oppen, Phys. Rev. Lett. **105**, 177002 (2010).

[8] H. M. Weng, C. Fang, Z. Fang, B. A. Bernevig, and X. Dai, Phys. Rev. X **5**, 011029 (2015).

[9] F. Dettwiler, J. Fu, S. Mack, P. J. Weigele, J. C. Egues, D. D. Awschalom, and D. M. Zumbühl, Phys. Rev. X **7**, 031010 (2017).

[10] J. Schliemann, J. C. Egues, and D. Loss, Phys. Rev. Lett. **90**, 146801 (2003).

[11] B. A. Bernevig, J. Orenstein, and S. C. Zhang, Phys. Rev. Lett. **97**, 236601 (2006).

[12] J. D. Koralek, C. P. Weber, J. Orenstein, B. A. Bernevig, S. C. Zhang, S. Mack, and D. D. Awschalom, Nature (London) **458**, 610 (2009).

[13] M. P. Walser, C. Reichl, W. Wegscheider, and G. Salis, Nat. Phys. **8**, 757 (2012).

[14] J. Fu, P. H. Penteado, M. O. Hachiya, D. Loss, and J. C. Egues, Phys. Rev. Lett. **117**, 226401 (2016).

[15] J. Fu and J. C. Egues, Phys. Rev. B **91**, 075408 (2015).

[16] R. Winkler, *Spin-Orbit Coupling Effects in Two-Dimensional Electron and Hole Systems* (Springer, Berlin, 2003)

[17] Y. A. Bychkov and E. I. Rashba, Pis'ma Zh. Eksp. Teor. Fiz. **39**, 66 (1984) [Sov. Phys. JETP Lett. **39**, 78 (1984)].

[18] G. Dresselhaus, Phys. Rev. **100**, 580 (1955).

[19] E. Bernardes, J. Schliemann, M. Lee, J. C. Egues, and D. Loss, Phys. Rev. Lett. **99**, 076603 (2007).

[20] R. S. Calsaverini, E. Bernardes, J. C. Egues, and D. Loss, Phys. Rev. B **78**, 155313 (2008).

[21] E. I. Rashba and V. I. Sheka, Fiz. Tverd. Tela: Collected Papers **2**, 162 (1959).

[22] G. Bihlmayer, O. Rader, and R. Winkler, New J. Phys. **17**, 050202 (2015).

[23] W. T. Wang, C. L. Wu, S. F. Tsay, M. H. Gau, I. Lo, H. F. Kao, D. J. Jang, J. C. Chiang, M. E. Lee, Y. C. Chang, C. N. Chen, and H. C. Hsueh, Appl. Phys. Lett. **91**, 082110 (2007).

[24] J. Y. Fu and M. W. Wu, J. Appl. Phys. **104**, 093712 (2008).

[25] W. Weber, S. D. Ganichev, S. N. Danilov, D. Weiss, W. Prettl, Z. D. Kvon, V. V. Belkov, L. E. Golub, H. I. Cho, and J. H. Lee, Appl. Phys. Lett. **87**, 262106 (2005).

[26] S. Schmult, M. J. Manfra, A. Punnoose, A. M. Sergent, K. W. Baldwin, and R. J. Molnar, Phys. Rev. B **74**, 033302 (2006).

[27] N. Thillosen, Th. Schäpers, N. Kaluza, H. Hardtdegen, and V. A. Guzenko, Appl. Phys. Lett. **88**, 022111 (2006).

[28] C. Kurdak, N. Biyikli, Ü. Özgür, H. Morkoç, and V. I. Litvinov, Phys. Rev. B **74**, 113308 (2006).

[29] I. Lo, M. H. Gau, J. K. Tsai, Y. L. Chen, Z. J. Chang, W. T. Wang, J. C. Chiang, T. Aggerstam, and S. Lourdudoss, Phys. Rev. B **75**, 245307 (2007).

[30] A. E. Belyaev, V. G. Raicheva, A. M. Kurakin, N. Klein, and S. A. Vitusevich, Phys. Rev. B **77**, 035311 (2008).

[31] E. B. Olshanetsky, Z. D. Kvon, S. Sassine, J. C. Portal, H. I. Cho, and J. H. Lee, Appl. Phys. Lett. **92**, 242112 (2008).

[32] H. Cheng, N. Biyikli, Ü. Özgür, C. Kurdak, H. Morkoç, and V. I. Litvinov, Physica E **40**, 1586 (2008).

[33] S. B. Lisesivdin, N. Balkan, O. Makarovsky, A. Patane, A. Yildiz, M. D. Caliskan, M. Kasap, S. Ozcelik, and E. Ozbay, J. Appl. Phys. **105**, 093701 (2009).

[34] W. Stefanowicz, R. Adhikari, T. Andrearczyk, B. Faina, M. Sawicki, J. A. Majewski, T. Dietl, and A. Bonanni, Phys. Rev. B **89**, 205201 (2014).

[35] L. C. Lew Yan Voon, M. Willatzen, M. Cardona, and N. E. Christensen, Phys. Rev. B **53**, 10703 (1996).

[36] V. I. Litvinov, Phys. Rev. B **68**, 155314 (2003).

[37] N. Thillosen, S. Cabañas, N. Kaluza, V. A. Guzenko, H. Hardtdegen, and Th. Schäpers, Phys. Rev. B **73**, 241311(R) (2006).

[38] E. I. Rashba, Sov. Phys. Solid State **1**, 368 (1959).

[39] V. Litvinov, *Wide Band Gap Semiconductor Spintronics* (Pan Stanford, Boca Raton, FL, 2016).

[40] S. L. Chuang and C. S. Chang, Phys. Rev. B **54**, 2491 (1996).

[41] C. Yin, B. Shen, Q. Zhang, F. J. Xu, N. Tang, L. B. Cen, X. Q. Wang, Y. H. Chen, and J. L. Yu, Appl. Phys. Lett. **97**, 181904 (2010).

[42] P. E. Faria Junior, T. Campos, C. M. O. Bastos, M. Gmitra, J. Fabian, and G. M. Sipahi, Phys. Rev. B **93**, 235204 (2016).

[43] J. A. Majewski, Acta Phys. Polonica A **108**, 777 (2005).

[44] V. I. Litvinov, Appl. Phys. Lett. **89**, 222108 (2006).

[45] M. Li, Y. H. Lv, B. H. Yang, Z. Y. Zhao, G. Sun, D. D. Miao, and C. Z. Zhao, Solid State Commun. **151**, 1958 (2011).

[46] P. Löwdin, J. Phys. Chem. **19**, 1396 (1951).

[47] M. Li, R. Zhang, Z. Zhang, B. Liu, D. Y. Fu, C. Z. Zhao, Z. L. Xie, X. Q. Xiu, and Y. D. Zheng, Phys. Status Solidi B **248**, 187 (2011).

[48] M. Cardona, N. E. Christensen, and G. Fasol, Phys. Rev. B **38**, 1806 (1988).

[49] The bulk contribution to the Rashba coupling in our wells, essentially refers to *weighted* (i.e., averaged) bulk contributions from both the well and barrier layers.

[50] A. Wolos, Z. Wilamowski, C. Skierbiszewski, A. Drabinska, B. Lucznik, I. Grzegory, and S. Porowski, Physica B **406**, 2548 (2011).

[51] J. A. Majewski and P. Vogl, AIP Conf. Proc. **772**, 1403 (2005).

[52] P. I. Tamborenea, T. Wellens, D. Weinmann, and R. A. Jalabert, Phys. Rev. B **96**, 125205 (2017).

[53] E. Q. Kane, J. Phys. Chem. Solids. **1**, 249 (1957).

[54] L. C. Lew Yan Voon and M. Willatzen, *The k·p Method— Electronic Properties of Semiconductors* (Springer, New York, 2009).

[55] G. L. Bir and G. E. Pikus, *Symmetry and Strain-Induced Effects in Semiconductors* (John Wiley and Sons, New York, 1974).

[56] T. B. Bahder, Phys. Rev. B **41**, 11992 (1990).

[57] R. C. Casella, Phys. Rev. **114**, 1514 (1959).

[58] Here we consider only the first conduction band given by the double group irreducible representation $\Gamma_7 = \Gamma_1 \otimes \Gamma_7$, which is the case, for example, for the group III nitride family (GaN), CdSe, and ZnO. However, for the wurtzite phase of GaSb, GaAs [59,60] and GaP [61], the Γ_7 and Γ_8 conduction bands are inverted and a different model might be necessary.

[59] M. Gmitra and J. Fabian, Phys. Rev. B **94**, 165202 (2016).

[60] A. Senichev, P. Corfdir, O. Brandt, M. Ramsteiner, S. Breuer, J. Schilling, L. Geelhaar, and P. Werner, Nano Res. **11**, 4708 (2018).

[61] A. Belabbes and F. Bechstedt, Phys. Status Solidi B **256**, 1800238 (2019).

[62] This procedure is equivalent to including only first order terms in the Löwdin expansion [16].

[63] G. B. Ren, Y. M. Liu, and P. Bloodb, Appl. Phys. Lett. **74**, 1117 (1999).

[64] M. J. Reed, N. A. Masry, C. A. Parker, J. C. Roberts, and S. M. Bedair, Appl. Phys. Lett. **77**, 4121 (2000).

[65] J. S. Im, H. Kollmer, J. Off, A. Sohmer, F. Scholz, and A. Hangleiter, Phys. Rev. B **57**, R9435 (1998).

[66] I. Vurgaftman, J. R. Meyer, and L. R. Ram-Mohan, J. Appl. Phys. **89**, 5815 (2001).

[67] W. Shan, R. J. Hauenstein, A. J. Fischer, J. J. Song, W. G. Perry, M. D. Bremser, R. F. Davis, and B. Goldenberg, Phys. Rev. B **54**, 13460 (1996).

[68] G. Bastard, *Wave Mechanics Applied to Semiconductor Heterostructures* (Halsted, Les Ulis, France, 1988).

[69] M. G. Burt, Semicond. Sci. Technol. **3**, 739 (1988).

[70] O. Ambacher, J. Majewski, C. Miskys, A. Link, M. Hermann, M. Eickhoff, M. Stutzmann, F. Bernardini, V. Fiorentini, V. Tilak, B. Schaff, and L. F. Eastman, J. Phys.: Condens. Matter **14**, 3399 (2002).

[71] J. Majewski, G. Zandler, and P. Vogl, J. Phys.: Condens. Matter **14**, 3511 (2002).

[72] N. Grandjean, B. Damilano, S. Dalmasso, M. Leroux, M. Laügt, and J. Massies, J. Appl. Phys. **86**, 3714 (1999).

[73] G. Martin, A. Botchkarev, A. Rockett, and H. Morkoç, Appl. Phys. Lett. **68**, 2541 (1996).

[74] T. H. Yu and K. F. Brennan, J. Appl. Phys. **89**, 3827 (2001).

[75] Since $V_e = V_H + \delta_e h_w(z)$ and $V_B = V_H - \delta_B h_w(z)$ (see Sec. II C), we have $V_e - V_B = (\delta_e + \delta_B)h_w(z)$. Therefore,

for $|z| < L_w/2$, $h_w(z) = 0$, and $\eta(z) = 2P_2\Delta_{sz}/(E_g + 2\Delta_2) = \alpha_{bulk}^{BIA}$; for $|z| > L_w/2$, $h_w(z) = 1$, and $\eta(z) = [2P_2\Delta_{sz}/(E_g + 2\Delta_2)][1 - (\delta_e + \delta_B)/(E_g + 2\Delta_2)]$, which is exactly the Taylor expansion of $\alpha_{bulk}^{BIA(b)} = 2P_2\Delta_{sz}/(E_g + 2\Delta_2 + \delta_e + \delta_B)$ (bulk Rashba coefficient for the barrier), up to the second order in $(\delta_e + \delta_B)/(E_g + 2\Delta_2)$.

[76] D. J. Dugdale, S. Brand, and R. A. Abram, Phys. Rev. B **61**, 12933 (2000).

[77] A. Dargys, Phys. Rev. B **72**, 045220 (2005).

[78] J. J. Sakurai, *Advanced Quantum Mechanics* (Addison-Wesley, Reading, MA, 1967).

[79] M. W. Wu, J. H. Jiang, and M. Q. Weng, Phys. Rep. **493**, 61 (2010).

[80] W.-T. Wang, C. L. Wu, J. C. Chiang, I. Lo, H. F. Kao, Y. C. Hsu, W. Y. Pang, D. J. Jang, M.-E. Lee, Y.-C. Chang, and C.-N. Chen, J. Appl. Phys. **108**, 083718 (2010).

[81] N. J. Harmon, W. O. Putikka, and R. Joynt, Appl. Phys. Lett. **98**, 073108 (2011).

[82] S. D. Ganichev and L. E. Golub, Phys. Status Solidi B **251**, 1801 (2014).

[83] S. H. Park and S. L. Chuang, Appl. Phys. Lett. **76**, 1981 (2000).

[84] E. P. Pokatilov, D. L. Nika, V. M. Fomin, and J. T. Devreese, Phys. Rev. B **77**, 125328 (2008).

[85] A. Polian, M. Grimsditch, and I. Grzegory, J. Appl. Phys. **79**, 3343 (1996).

[86] The s.–p_z mixing modifies the S (conduction subband) and the Z (valence band) wave functions, which can be written

as $|S\rangle \rightarrow |S'\rangle = q_s|S\rangle + q_z|Z\rangle$ and $|Z\rangle \rightarrow |Z'\rangle = q_s|Z\rangle - q_z|S\rangle$, with $q_s^2 + q_z^2 = 1$ [35]. Based on the new wave functions and the definition of Δ_{sz} by Eq. (8), one can straightforwardly obtain $\Delta_{sz} = q_z\Delta_3$. Here we consider $q_z = 0.1$.

[87] O. Ambacher, J. Smart, J. R. Shealy, N. G. Weimann, K. Chu, M. Murphy, W. J. Schaff, L. F. Eastman, R. Dimitrov, L. Wittmer, M. Stutzmann, W. Rieger, and J. Hilsenbeck, J. Appl. Phys. **85**, 3222 (1999).

[88] Q. M. Yan, P. Rinke, M Winkelnkemper, A. Qteish, D. Bimberg, M. Scheffler, and C. G. Van de Walle, Semicond. Sci. Technol. **26**, 014037 (2011).

[89] S. H. Park and S. L. Chuang, Appl. Phys. Lett. **72**, 3103 (1998).

[90] A. S. Barker, Jr. and M. Ilegems, Phys. Rev. B **7**, 743 (1973).

[91] S. H. Park and S. L. Chuang, J. Appl. Phys. **87**, 353 (2000).

[92] H. M. Ng, R. Harel, S. N. G. Chu, and A. Y. Cho, J. Elec. Mater. **30**, 134 (2001).

[93] M. I. Aroyo, J. M. Perez-Mato, D. Orobengoa, E. Tasci, G. de la Flor, and A. Kirov, Bulg. Chem. Commun. **43**, 183 (2011).

[94] M. I. Aroyo, J. M. Perez-Mato, C. Capillas, E. Kroumova, S. Ivantchev, G. Madariaga, A. Kirov, and H. Wondratschek, Z. Kristallogr. **221**, 15 (2006).

[95] M. I. Aroyo, A. Kirov, C. Capillas, J. M. Perez-Mato, and H. Wondratschek, Acta Cryst. A **62**, 115 (2006).

[96] D. Varjas, T. Ö. Rosdahl, and A. R. Akhmerov, New J. Phys. **20**, 093026 (2018).